Check for updates

Paleoceanography and Paleoclimatology

RESEARCH ARTICLE
10.1029/2020PA004137

Key Points:

- Coherent dust flux changes along the NW African margin and in the central North Atlantic over the last 67 ka
- Abrupt dust flux variations on millennial timescales similar to N Atlantic stadials related to high-latitude forcing of African climate
- Green Sahara interval (60–50 ka) recorded by low dust fluxes to ODP 658C showing an orbitally forced strengthening of monsoon during MIS 3

Supporting Information:

Supporting Information may be found in the online version of this article.

Correspondence to:

C. W. Kinsley,
ckinsley@mit.edu

Citation:

Kinsley, C. W., Bradtmiller, L. I., McGee, D., Galgay, M., Stuut, J.-B., Tjallingii, R., et al. (2022). Orbital- and millennial-scale variability in Northwest African dust emissions over the past 67,000 years. *Paleoceanography and Paleoclimatology*, *37*, e2020PA004137. https://doi.org/10.1029/2020PA004137

Received 2 OCT 2020
Accepted 11 OCT 2021

Orbital- and Millennial-Scale Variability in Northwest African Dust Emissions Over the Past 67,000 years

Christopher W. Kinsley[1], **Louisa I. Bradtmiller**[2], **David McGee**[1], **Michael Galgay**[2], **Jan-Berend Stuut**[3,4], **Rik Tjallingii**[5], **Gisela Winckler**[6], **and Peter B. deMenocal**[6,7]

[1]Department of Earth, Atmospheric and Planetary Sciences, Massachusetts Institute of Technology, Cambridge, MA, USA, [2]Department of Environmental Studies, Macalester College, St. Paul, MN, USA, [3]NIOZ Royal Netherlands Institute for Sea Research, Texel, The Netherlands, [4]Faculty of Science, Department of Earth Sciences, Vrije Universiteit Amsterdam, Amsterdam, The Netherlands, [5]GFZ German Research Centre for Geosciences, Section 'Climate Dynamics and Landscape Evolution', Potsdam, Germany, [6]Lamont-Doherty Earth Observatory, Columbia University, Palisades, NY, USA, [7]Woods Hole Oceanographic Institution, Woods Hole, MA, USA

Abstract Reconstructions of aeolian dust flux to West African margin sediments can be used to explore changing atmospheric circulation and hydroclimate over North Africa on millennial to orbital timescales. Here, we extend West African margin dust flux records back to 37 ka in a transect of sites from 19° to 27°N, and back to 67 ka at Ocean Drilling Program (ODP) Hole 658C, in order to explore the interplay of orbital and high-latitude forcings on North African climate and make quantitative estimates of dust flux during the core of the Last Glacial Maximum (LGM). The ODP 658C record shows a Green Sahara interval from 60 to 50 ka during a time of high Northern Hemisphere summer insolation, with dust fluxes similar to levels during the early Holocene African Humid Period, and an abrupt peak in flux during Heinrich event 5a (H5a). Dust fluxes increase from 50 to 35 ka while the high-latitude Northern Hemisphere cools, with peaks in dust flux associated with North Atlantic cool events. From 35 ka through the LGM dust deposition decreases in all cores, and little response is observed to low-latitude insolation changes. Dust fluxes at sites from 21° to 27°N were near late Holocene levels during the LGM time slice, suggesting a more muted LGM response than observed from mid-latitude dust sources. Records along the northwest African margin suggest important differences in wind responses during different stadials, with maximum dust flux anomalies centered south of 20°N during H1 and north of 20°N during the Younger Dryas.

Plain Language Summary Dust that is picked up by winds over North Africa and blown out into the Atlantic Ocean can tell us about climate change in the past, particularly about variations in wind strength and location, and how wet the continent was. This study uses seafloor sediments from four sites offshore of West Africa to reconstruct how much dust was blown out from North Africa over the last 67,000 years. The records show that the climate of North Africa is controlled by two major processes: changes to incoming energy from the sun on timescales of thousands of years, and the extent of cold conditions in the high latitudes of the North Atlantic region on timescales of hundreds of years. We find a time from 60,000 to 50,000 years ago of low dust export (weak winds and a wet continent) when incoming energy from the sun was high, with dust levels similar to those during the Green Sahara interval that occurred 11,000 to 5,000 years ago. This time of low dust export was interrupted around 54,500 years ago by a brief interval of extremely high dust export (strong winds and a dry continent) during a North Atlantic cold interval called Heinrich event 5a.

1. Introduction

Records of mineral dust emissions from the Sahara Desert are essential for understanding past changes in North African climate, and are tightly linked to the strength of the West African monsoon (deMenocal, 1995; deMenocal, Ortiz, Guilderson, Adkins, et al., 2000; deMenocal, Ortiz, Guilderson, & Sarnthein, 2000; Skonieczny et al., 2019; Wang, et al., 2015). Wind speed and aridity variations are expressed as fluctuations in the amount of dust exported from the North African continent to the Atlantic Ocean, meaning that downcore measurement of dust flux to North Atlantic sediments allows an integrated reconstruction of how winds and aridity respond to climate changes.

In the present day, North African dust outbreak events transport dust over the northwest African continental margin and Atlantic Ocean throughout the year, with a shift in transport pathway across the Atlantic from north in summer (centered ~18°N) to south in winter (centered ~6°N) (Meng et al., 2017). Observational records from marine sediment traps and atmospheric dust samplers suggest that maximum dust deposition along the northwest African margin occurs in winter and spring (Bory & Newton, 2000; Chiapello et al., 1995; Ratmeyer et al., 1999; Skonieczny et al., 2013). Combining air parcel back trajectory modeling with dust provenance (Friese et al., 2017; Skonieczny et al., 2013) and grain size measurements (van der Does et al., 2016) suggests that winter dust is transported in low-level trade winds from relatively proximal locations, including the coastal region of Western Sahara and western Mauritania (see Scheuvens et al., 2013 for a compilation of PSA locations). Interannual peaks in winter dust emissions are attributed to southward movement of the ITCZ and increased surface winds over North African dust source regions, with a minor role of reduced Sahel rainfall (Doherty et al., 2012).

During summer, dust is transported from source regions closer to the center of the continent (e.g., Libya) and uplifted at the coast by a cool marine inversion layer and transported by the upper level (~1.5–4.5 km) Saharan Air Layer (Carlson & Prospero, 1972). Satellite observations of atmospheric dust loading and fluxes show peak dust transport across the Atlantic in summer (Ridley et al., 2012; Yu et al., 2015); however, relatively little of this dust appears to be deposited on the northwest African margin (Skonieczny et al., 2013). As a result, our records are likely to be biased toward winter dust emissions from the western Sahara Desert. To address this potential seasonal and spatial bias in our interpretations, in Section 4.1 we compare data from our African margin sites with data from a distal core site that represents predominantly summer dust deposition from interior African source regions (Middleton et al., 2018).

Paleoclimate proxy records and geochemical tools have been used to extend the record of variability of dust transport to the margin beyond the observational record, which exists only from the mid-1960s (Prospero & Lamb, 2003). Records of the last 20 ka (ka: thousand years before present) were developed using sediments from Ocean Drilling Program (ODP) Hole 658C by deMenocal, Ortiz, Guilderson, Adkins, et al. (2000), deMenocal, Ortiz, Guilderson, and Sarnthein (2000), and Adkins et al. (2006). Later work demonstrated that the variations in this core were coherent along the northwest African margin between 19°N and 27°N (McGee et al., 2013) and were observed across the Atlantic Basin in the central Atlantic and Bahamas as well (Williams et al., 2016). These reconstructions show an abrupt transition from a time of high dust accumulation during the deglaciation to a sustained period of low dust accumulation between 11 and 5 ka. This low-dust period is known as the African Humid Period (AHP) and is marked by an abrupt onset and termination, followed by a more gradual increase of dust accumulation toward the present. Comparison of these dust records with other climate proxy records of North African climate shows that the AHP marks a Green Sahara interval, when the Sahara Desert received high rainfall supporting diverse and widespread vegetation, permanent lakes, and human populations (McGee & deMenocal, 2017, and references therein), with accompanying continental runoff (Drake et al., 2010; Skonieczny et al., 2015; Weldeab et al., 2014). The AHP occurred when Northern Hemisphere summer insolation was increased relative to the present due to precessional variation, which has been shown through modeling efforts to increase the extent and intensity of the monsoon system (Battisti et al., 2014; Braconnot et al., 2012; Kutzbach, 1981; Tjallingii et al., 2008). There is also evidence that trade wind strength was decreased over the West African margin during the AHP, as evidenced by decreased upwelling-related biogenic fluxes to margin sediments and increased sea surface temperatures (SSTs) along the margin (Adkins et al., 2006; Bradtmiller et al., 2016). These findings over the AHP highlight two of the controls on changes to dust flux from North Africa, aridity and wind strength, and the importance of considering the interplay between the two.

The paleoclimate records developed along the West African margin also began to elucidate dramatic intervals of rapid and high-amplitude changes to climate and dust transport to the margin over far shorter timescales, punctuating the orbitally forced record at a millennial scale. During abrupt Northern Hemisphere cooling events such as Heinrich event 1 (H1) (18.0–15.6 ka; Sánchez Goñi & Harrison, 2010), and the Younger Dryas (YD) episode (12.8–11.7 ka; Rasmussen et al., 2006) abrupt increases in dust flux have been recorded at multiple sites over the margin, with fluxes reaching the highest values of their respective records during these events (Adkins et al., 2006; McGee et al., 2013; Mulitza et al., 2008).

Multiple studies have linked North Atlantic cooling to increases in northeasterly winds over North Africa (deMenocal et al., 1993; McGee et al., 2018; Meyer et al., 2013; Mulitza et al., 2008; Tjallingii et al., 2008). Cooling of winter SSTs and expansion of sea ice in the North Atlantic shift the Atlantic ITCZ to the south, weakening the monsoon and increasing trade wind strength, leading to an increase of dust export (Liu et al., 2014; Murphy et al., 2014). Consistent with this finding from models, northwest African margin sediments record increases in the accumulation of biogenic opal and organic carbon during these cold events, suggesting increased wind-driven upwelling (Adkins et al., 2006; Bradtmiller et al., 2016; Romero et al., 2008). A weakening of monsoon rainfall during North Atlantic cooling events also shifts the Sahel-Sahara boundary south (Collins et al., 2013), potentially opening up new dust source areas and further contributing to the increase in dust emissions during these events. These high-resolution studies provide evidence for a North Atlantic high-latitude control causing abrupt changes to atmospheric circulation and North African climate on millennial timescales, in addition to the low-latitude orbital regulation of African monsoonal climate.

Recent efforts by Skonieczny et al. (2019) have shown a high correlation of Saharan dust flux, calculated using ^{230}Th-normalization, with summer insolation from 240 ka to present, confirming low-latitude pacing of northwest African dust fluxes at 18°N spanning at least the last two glacial cycles for sediment core MD03-2705. Here we present northwest African margin dust flux records to explore the combined effects of high-latitude and orbital forcing of African climate extending back to 67 ka. Probing this time period allows us to examine over multiple precessional cycles the impact of high-latitude and summer insolation forcing on dust export, and to provide quantitative estimates of dust flux during the core of the Last Glacial Maximum (LGM) time slice. We also explore how millennial-scale increases in dust emission varied along a north-south transect of cores, providing insight into the spatial distribution of wind and aridity changes during these events. Drawing on the mechanistic links between regional climate and dust export, we aim to deepen understanding of changing climate of the North Africa region from 67 ka to present.

2. Methods and Core Sites

2.1. Core Locations

A meridional transect of 4 core sites between 27° and 19°N were used in this study (Figure 1). These sites have been used to monitor past variations in northwest African climate (Bradtmiller et al., 2016; McGee et al., 2013; Williams et al., 2016), as they represent North African dust emissions to the tropical North Atlantic. The three gravity cores GC37, GC49, and GC68, were taken by the R/V Oceanus during the 2007 Changing Holocene Environments of the Eastern Tropical Atlantic (CHEETA) cruise (OC437-7). The sediments from Ocean Drilling Program Hole 658C off Cap Blanc, Mauritania were cored during ODP Leg 108 (Ruddiman et al., 1988).

2.2. Age Models

The chronologies for the CHEETA cores were developed from existing AMS radiocarbon ages from GC37, GC49, and GC68, taken from McGee et al. (2013) and Tierney, Pausata, and deMenocal (2017) (see Figure S1 in Supporting Information S1). Radiocarbon ages were converted to calendar ages using Marine13 (Reimer et al., 2013), with an additional reservoir correction (ΔR) of 130 ± 50 years (2σ) based upon local modern reservoir ages (Mulitza et al., 2010; Ndeye, 2008; Pittauerov et al., 2009). We do not attempt to estimate past changes in reservoir age, though these most certainly accompanied the dramatic changes in upwelling observed in African margin records (Bradtmiller et al., 2016; Romero et al., 2008). Age models were interpolated between ^{14}C tie points using the P_Sequence routine in OxCal 4.2 (Bronk Ramsey, 2008). This routine provides Bayesian age-depth modeling and treats sediment deposition as a series of discrete "events" following a Poisson distribution with a user-specified step size. A step size (k) of 0.75 cm^{-1} provided sufficient flexibility in the age-depth relationship to fit our ^{14}C ages.

The chronology for the ODP 658C core is based on AMS radiocarbon ages and correlation to a geochemical record from a nearby core with existing age model (see Supporting Information Figure S2a in Supporting Information S1). From 20 ka to the coretop radiocarbon ages from deMenocal, Ortiz, Guilderson, Adkins, et al. (2000) and deMenocal, Ortiz, Guilderson, and Sarnthein (2000) are utilized, and two new radiocarbon ages were measured for this study to constrain the chronology from 38.5 to 30 ka. The ages for this study were determined on planktonic foraminiferal calcium carbonate tests (of *Globigerina bulloides*), which were sonicated in deionized water to reduce sedimentary contamination prior to submission to the Center for Accelerator Mass Spectrometry at Lawrence Livermore National Laboratory for radiocarbon measurement. The pre-existing and new radiocarbon ages were calibrated using Marine13 and a reservoir correction (ΔR) of 130 ± 50 years (2σ), in keeping with the treatment of the CHEETA cores. Between 67 and 24 ka the chronology is also constrained by matching $CaCO_3$ weight percent in ODP 658C to calibrated XRF $CaCO_3$ weight percent in neighboring core GeoB7920-2 (see

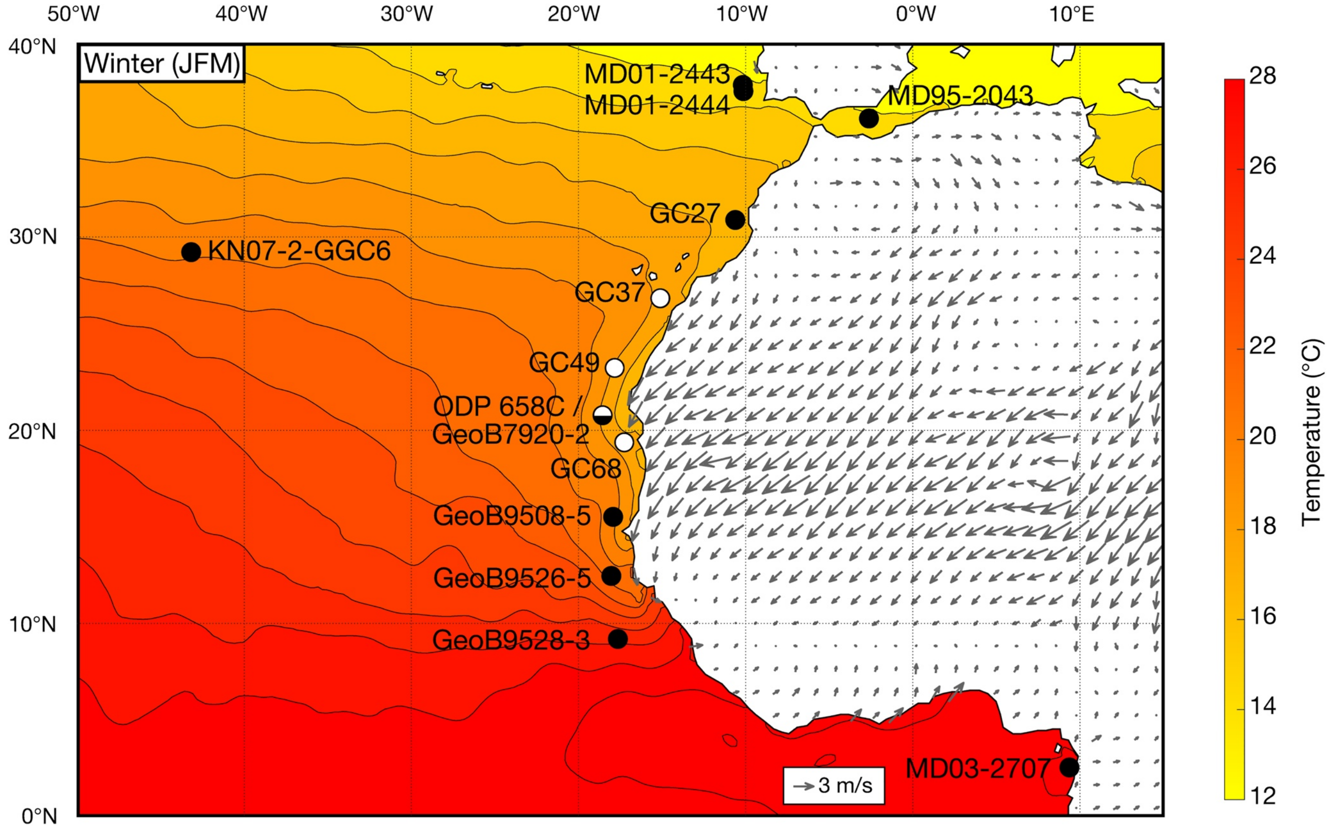

Figure 1. Location map of studied core sites and modern winter (JFM) SSTs and surface winds. Winter (JFM) SSTs from the WOA18 (black contours; Locarnini et al., 2019) and 10 m winds from ERA5 (gray arrows; C3S, 2017). Studied core locations (white circles) and water depths as follows: GC37 (26°48.96'N, 15°7.06'W, 2771 m), GC49 (23°12.37'N, 17°51.25'W, 2303 m), ODP 658C (20°44.95'N, 18°34.85'W, 2263.6 m), and GC68 (19°21.78'N, 17°16.94'W, 1,396 m). Additional core sites referenced in this study are shown by black circles.

Figure S2b in Supporting Information S1). The age model for this part of GeoB7920-2 is based on visual correlation of the benthic (*Cibicidoides wuellerstorfi*) $\delta^{18}O$ record with that of marine sediment core MD95-2042, with the $\delta^{18}O$ stratigraphy of MD95-2042 on the GRIP ss09sea age scale (Tjallingii et al., 2008).

2.3. Determination of Biogenic Components and Aeolian Fraction of Sediments

The percentages of the biogenic components of the sediments (calcium carbonate, organic carbon, and opal) were measured at Macalester College. Percent calcium carbonate was measured by acidification coulometry. Samples were reacted with acid in a UIC CM5240 acidification module, and the resulting CO_2 was measured by quantitative titration in a UIC CM5015 coulometer. Total carbon was measured by combustion in a UIC CM5200 furnace module, with the resulting CO_2 again measured by quantitative titration in a UIC CM5015 coulometer. Organic carbon was calculated as the difference between total carbon and calcium carbonate carbon. Percent biogenic opal was determined using alkaline extraction and molybdate blue spectrophotometry after the method of Mortlock and Froelich (1989).

The aeolian fraction of the sediments was calculated by utilizing endmember modeling of the grain size distributions of the detrital fraction of the sediments in order to separate aeolian from hemipelagic inputs. The detrital percentage of the samples was calculated as the residual after subtracting the measured biogenic component percentages, and was isolated using a stepwise leaching procedure. Organic matter and calcium carbonate were removed in a glass beaker using excess 10% hydrogen peroxide and 0.1 M hydrochloric acid, respectively. Opal was removed by transferring the samples to centrifuge tubes, adding excess 2 M sodium carbonate, and heating the samples in an 85°C hot bath for 5 hr. Grain size measurements on the detrital fraction were made on a Beckman Coulter LS 13320 Laser Diffraction Particle Size Analyzer at the Royal Netherlands Institute for Sea

Research. The grain size data for each site were fit by Weibull distributions, which are unimodal, asymmetric distributions that closely approximate measured grain size distributions of airborne dust and loess (Sun, 2004; Zobeck et al., 1999). Three endmembers per site were used to model the grain size distributions, with the two coarsest endmembers identified as aeolian dust, following the work of McGee et al. (2013). The proportion of the grain size distribution that was accounted for by the two coarsest endmembers was taken as the fraction of the detrital material that is aeolian, and this value was multiplied by the detrital percentage to obtain the aeolian fraction of the bulk sediments.

This approach derives from multiple studies showing that the grain size distributions of the detrital fraction of northwest African margin sediments can be approximated well by three endmembers (Holz et al., 2004, 2007; McGee et al., 2013; Mulitza et al., 2008; Tjallingii et al., 2008); that the two coarser endmembers are similar in grain size to modern-day dust collected by dust traps (Stuut et al., 2005); and that the finest endmember peaks in abundance near river mouths (Holz et al., 2004) and varies in flux independently from the other two endmembers (McGee et al., 2013). The same endmember distributions that McGee et al. (2013) calculated for cores GC37, GC49, and GC68 were utilized to estimate aeolian fractions for new sediment samples from those sites in this study. The average root-mean-square (RMS) deviation between the modeled and measured grain size distributions of the new samples for cores GC37 and GC49 were within 0.01% points of the average RMS deviations for each of these cores found by McGee et al. (2013), and within 0.05% points for core GC68. For core ODP 658C best fit endmember Weibull distributions were calculated from grain size distribution data on all samples analyzed in this study (from 67 to 19 ka), which are broadly consistent with the CHEETA endmembers and nearby modern-day dust (see Figure S3 in Supporting Information S1), and used to estimate the aeolian fraction of the sediments.

2.4. U, Th Isotope Measurements

Aeolian fluxes were calculated by multiplying the aeolian fraction of the sediments by the vertical sediment flux. Sediment fluxes were calculated using ^{230}Th-normalization (Bacon, 1984; Suman & Bacon, 1989), which utilizes the fact that the instantaneous ratio of water column scavenged ^{230}Th flux to the total sediment flux must be equal to the concentration of ^{230}Th in the underlying sediment:

$$\text{normalized aeolian flux} = \frac{\beta z}{[^{230}Th^0_{xs}]} F \tag{1}$$

where β is the production rate of ^{230}Th from ^{234}U in the water column (0.0268 dpm m^{-3} yr^{-1}, McGee et al., 2010), z is the water column depth (m), [$^{230}Th_{xs}{}^0$] is the concentration of the component of the total ^{230}Th$_{meas}$ that is not derived from detrital material or supported by ^{238}U decay within the sediments (in dpm/g), and has been corrected for decay since it was deposited, and F is the fraction of aeolian material. The water column depth was adjusted for changing sea level (Waelbroeck et al., 2002) as this affects the production rate of ^{230}Th in the water column.

^{230}Th$_{xs}{}^0$ is calculated using the following equation:

$$^{230}Th^0_{xs} = e^{\lambda_{230}t} \times [^{230}Th_{meas} - {}^{230}Th_{det} - {}^{230}Th_{auth}] \tag{2}$$

The correction for decay was made using the age model of the core to assign an age to each sample and account for the decay of initial excess ^{230}Th since the time of deposition. The detrital ^{230}Th was calculated by assuming the ^{232}Th content of the sample was entirely sourced from the detrital component, and calculating the activity of the ^{238}U associated with this detrital component using an estimated detrital ^{238}U/^{232}Th activity ratio of 0.7 ± 0.05 (1σ) for this area (Adkins et al., 2006). The detrital ^{230}Th is assumed to be in secular equilibrium with this uranium, so it can be subtracted from the ^{230}Th$_{meas}$. Authigenic uranium is taken to be that which remains after accounting for the detrital uranium. Authigenic ^{230}Th is therefore calculated by assuming that the formation of authigenic minerals/coatings occurs at the time of sediment deposition and incorporates ^{234}U/^{238}U at a constant seawater activity ratio of 1.1468 (Andersen et al., 2010).

In preparation for isotopic measurements samples were weighed, doped with a mixed spike of ^{229}Th and ^{236}U, and fully dissolved with hydrogen peroxide, nitric acid, hydrochloric acid, and hydrofluoric acid. An iron coprecipitation step allowed removal of much of the matrix of the dissolved sediments and thus improved yields of Th and U. Samples then underwent anion exchange chromatography using Dowex Bio-Rad AG1-X8 100–200 mesh anion exchange resin to separate Th and U so that the two elements could be measured separately. ^{230}Th, ^{232}Th, and ^{238}U isotope measurements were made using a multi-collector inductively coupled plasma source mass spectrometer (MC-ICP-MS). The majority of isotopic measurements were made using a ThermoScientific Neptune Plus MC-ICP-MS at Brown University; more recent measurements were made on a Nu Plasma II-ES MC-ICP-MS at MIT. Average full procedural blanks, with the maximum blank correction listed in brackets, were 67 fg of ^{230}Th (5.6%), 267 pg of ^{232}Th (<1%), and 337 pg of ^{238}U (<1%). The reported uncertainties reflect analytical uncertainties (associated with the measurement of the U and Th isotope composition, the percentages of the biogenic components, and the grain size distributions and endmember modeling) and uncertainty related to the estimated detrital ^{238}U/^{232}Th activity ratio. The reproducibility of ^{230}Th-based fluxes measured on an internal standard included in each set of samples was 4% RSD.

The uncertainties in fluxes do not incorporate uncertainties in the assumption that the supply of scavenged ^{230}Th to the sediment is equivalent to the production rate of ^{230}Th in the overlying water column. Our core sites lie in an exceptionally productive region of upwelling which can lead to boundary scavenging of ^{230}Th: there is strong year round upwelling from 20° to 26°N along the West African margin, with weaker year round upwelling north of 26°N, and seasonal upwelling south of 20°N (Gómez-Letona et al., 2017). Currently, boundary scavenging of ^{230}Th has been constrained to 40% ± 10% of its water column production off northwest Africa (Hayes et al., 2015), helping to quantify this additional uncertainty associated with ^{230}Th-normalized sediment fluxes in our study region. This scavenging would increase ^{230}Th deposition in sediments at our core sites, biasing our accumulation rates low. It is assumed that changes in anomalous ^{230}Th deposition due to changes in boundary scavenging are much smaller than the factor of >3 changes in flux seen in our records, meaning that relative changes in flux are likely to be robust even if the mean flux is biased low.

3. Results

The meridional sediment core transect along the northwest African margin reveals latitudinal differences in the relative expressions of low-latitude (orbital monsoon) and high-latitude (glacial and stadial event) forcing on regional dust fluxes and coastal upwelling (Figures 2 and 3). Dust, opal, and organic carbon fluxes for the <15 ka portion of GC37, <22 ka portion of GC49, and <20 ka portion of GC68 were previously published in McGee et al. (2013) and Bradtmiller et al. (2016). Calcium carbonate and opal percentages and sediment flux data for the <19 ka portion of ODP 658C were previously published in Adkins et al. (2006), deMenocal, Ortiz, Guilderson, Adkins, et al. (2000), and deMenocal, Ortiz, Guilderson, and Sarnthein (2000). The ages of global climate events discussed in the following text are taken from the literature as follows: AHP—Tierney, Pausata, and deMenocal (2017); YD—Rasmussen et al. (2006); LGM - Waelbroeck et al. (2009); H1-6 and marine isotope stage timing—Sánchez Goñi and Harrison (2010); H5a timing—Rashid et al. (2003); H5a relative timing—Seierstad et al. (2014).

3.1. GC37 (27°N)

Dust fluxes in core GC37 exhibit a maximum from 36 to 31 ka during late marine isotope stage (MIS) 3 (~0.5 g cm^{-2} kyr^{-1}), with a millennial-scale peak coincident with H3. Fluxes gradually fall during MIS 2 to moderately low values (0.26 g cm^{-2} kyr^{-1}) in the LGM, with a small dust peak associated with H2. Dust fluxes rise to millennial-scale peaks during H1 (0.37 g cm^{-2} kyr^{-1}) and the YD (0.47 g cm^{-2} kyr^{-1}), with the YD showing a 20% higher peak flux of dust than H1. Fluxes abruptly fall during the onset of the AHP, and continue to fall to the lowest recorded value at ~6 ka (0.09 g cm^{-2} kyr^{-1}). Dust fluxes then increase into the late Holocene to a value of ~0.3 g cm^{-2} kyr^{-1}.

Both opal and organic carbon fluxes are positively correlated with dust fluxes in core GC37 ($r^2 = 0.69$; p-value < 0.05 and $r^2 = 0.43$; p-value < 0.05, respectively). Similar to dust, both opal and organic carbon are at maximum levels at ~36 ka, the base of the core. Biogenic fluxes decrease into the LGM, with opal more closely tracking dust and organic carbon dropping rapidly after 30 ka. Opal fluxes rise to high levels during both H1 and the YD, while organic carbon fluxes peak only in H1. Fluxes of both opal and organic carbon fall to low levels throughout the AHP before rising during the late Holocene.

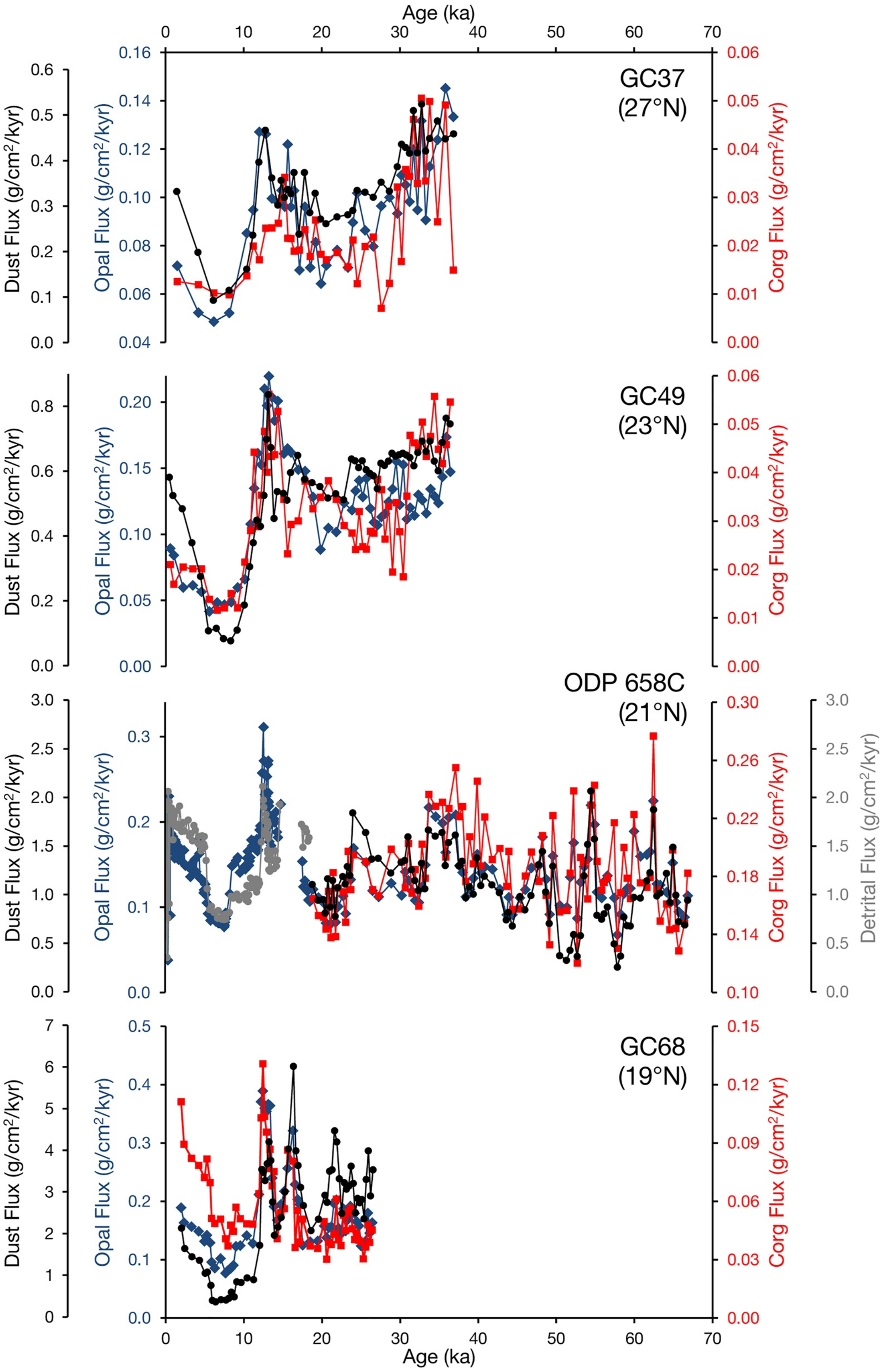

Figure 2. Biogenic and aeolian fluxes at each studied core site. Opal (blue diamonds), C_{org} (red squares), dust (black circles), and detrital (gray circles) flux records arranged from north to south as labeled. Data <15 ka in GC37, <22 ka in GC49, and <20 ka in GC68 from Bradtmiller et al. (2016) and McGee et al. (2013); data <19 ka in ODP 658C from Adkins et al. (2006), deMenocal, Ortiz, Guilderson, Adkins, et al. (2000), and deMenocal, Ortiz, Guilderson, and Sarnthein (2000).

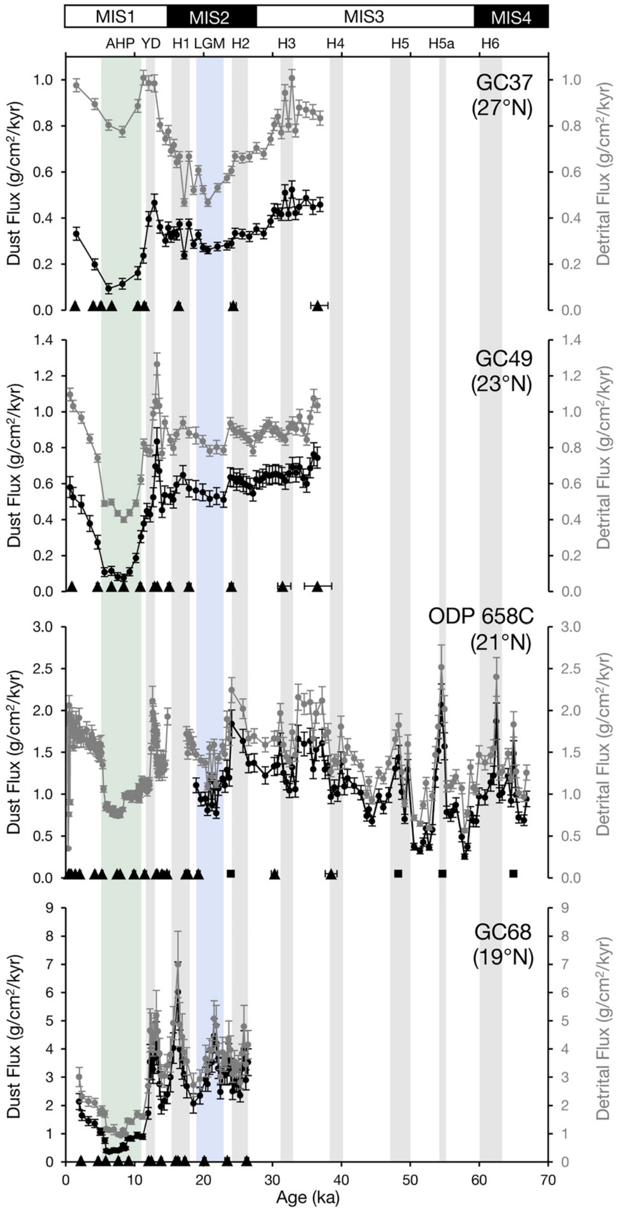

Figure 3. Detrital and aeolian fluxes at each studied core site. Dust (black circles) and detrital (gray circles) flux records arranged from north to south as labeled with 1σ uncertainties shown. ^{14}C tie points shown as black triangles with 1σ uncertainties, calcium carbonate stratigraphy tie points for ODP 658C shown as black squares. Flux data <15 ka in GC37, <22 ka in GC49, and <20 ka in GC68 from McGee et al. (2013); flux data <19 ka in ODP 658C from Adkins et al. (2006). ^{14}C tie points for GC37, GC49, and GC68 from McGee et al. (2013) and Tierney, Pausata, and deMenocal (2017); ^{14}C tie points <20 ka for ODP 658C from deMenocal, Ortiz, Guilderson, Adkins, et al. (2000) and deMenocal, Ortiz, Guilderson, and Sarnthein (2000). Vertical bars show time intervals of comparison between the records (AHP—Tierney, Pausata, & deMenocal, 2017; YD—Rasmussen et al., 2006; LGM—Waelbroeck et al., 2009; H1-6 and MIS timing—Sánchez Goñi & Harrison, 2010; H5a timing—Rashid et al., 2003; H5a relative timing—Seierstad et al., 2014).

3.2. GC49 (23°N)

Dust fluxes in core GC49 decrease steadily from a late MIS 3 maximum at 36 ka (0.74 g cm^{-2} kyr^{-1}) to moderately low values during the LGM (0.52 g cm^{-2} kyr^{-1}), with a small peak coincident with H2. Dust fluxes then rise to peaks during H1 (0.65 g cm^{-2} kyr^{-1}) and the YD (0.84 g cm^{-2} kyr^{-1}), before decreasing to a minimum during the AHP (0.08–0.11 g cm^{-2} kyr^{-1}). Similar to the GC37 record, the dust flux peak associated with the YD is larger—by ~30%—than the H1 peak, showing a stronger dust response during the YD in the northern core sites. Dust fluxes then increase into the late Holocene to a value of 0.58 g cm^{-2} kyr^{-1}.

Both opal and organic carbon fluxes are positively correlated with dust fluxes in core GC49 ($r^2 = 0.45$; p-value < 0.05 and $r^2 = 0.39$; p-value < 0.05, respectively). Opal and organic carbon fluxes are at high levels during late MIS 3 at ~36 ka, the end of the core, and both decrease into the LGM. Opal fluxes more closely track dust fluxes, also showing a peak coincident with H2, while the organic carbon fluxes drop rapidly after 30 ka and are highly variable during the early part of MIS 2. Opal fluxes rise to high levels during H1 and the YD, while organic carbon fluxes peak only in H1 and show an earlier peak during the LGM. Fluxes of both opal and organic carbon fall to low levels throughout the AHP before rising during the late Holocene.

3.3. GC68 (19°N)

Core GC68 provides the highest resolution dust fluxes in this study due to the high sediment accumulation rates at this site, which as the most southern site studied is the closest in the transect to the core of the Saharan summer and winter dust plume. The highest sedimentation rates are in the older portion of the core, from 26 to 12 ka, at a time when the average dust fraction of the detrital material is 81% (see Figure S4 in Supporting Information S1), meaning that we can dismiss other inputs, such as nearby paleorivers, as a major component of material at this site (Drake et al., 2010; Skonieczny et al., 2015). At the LGM low sea level stand GC68 would have been located only 30 km from the shoreline (McGee et al., 2013), with the potential for increased deposition of coarser shelf material. However we think that input of resuspended coarser shelf material is unlikely to be a major contributor to the coarse-grained fraction of sediments at GC68 during the LGM and subsequent sea level rise (see Text S1 in Supporting Information S1). From 26 ka to the end of the LGM, dust fluxes show a slight decrease punctuated by abrupt rises and falls between values of ~4.5 to ~2 g cm^{-2} kyr^{-1}, including a small peak coincident with H2 and a prominent peak at ~21.5 ka. Dust fluxes then rise to peaks during H1 (~6 g cm^{-2} kyr^{-1}) and the YD (~4.2 g cm^{-2} kyr^{-1}), before decreasing to a minimum during the AHP (0.39–0.49 g cm^{-2} kyr^{-1}). In contrast to cores GC37 and GC49, the H1 peak dust flux is larger than the YD peak dust flux (by ~50%), showing a stronger dust response during H1 at this southern core site. Dust fluxes then increase into the late Holocene to a value of 2.14 g cm^{-2} kyr^{-1}.

Opal fluxes are positively correlated with dust fluxes in core GC68 ($r^2 = 0.44$; p-value < 0.05), while organic carbon fluxes show very low correlation ($r^2 = 0.02$; p-value > 0.05). From 26 ka, the end of the core, to the end of the LGM opal fluxes show a slight decrease punctuated by abrupt rises and falls similar to the dust record, also recording peaks coincident with H2 and at ~21.5 ka. Organic carbon fluxes show a substantial difference from dust fluxes from 26 ka to the end of the LGM with no noticeable trend and high variability. Biogenic fluxes rise to high levels during both H1 and the YD, with the YD peak slightly larger than the H1 peak in both opal and organic carbon fluxes. Fluxes of both opal and organic carbon fall to low levels throughout the AHP before rising during the late Holocene.

3.4. ODP 658C (21°N)

The ODP 658C core provides a longer archive than the CHEETA cores and allows continued high-resolution study of dust accumulation rates to the margin. Here we extend the record back to 67 ka. The early portion of the record at the latter stages of MIS 4 shows moderate dust fluxes to the margin followed by an abrupt peak (1.9 g cm^{-2} kyr^{-1}) coincident with H6. This is followed by a decline in dust flux to an interval from 60–50 ka when the lowest dust fluxes (0.26 g cm^{-2} kyr^{-1}) observed in the record for this site are recorded. This low dust interval is interrupted by an abrupt (millennial-scale) dust increase to the highest fluxes (2.1 g cm^{-2} kyr^{-1}) observed in the whole record coincident with H5a. A trend of increasing dustiness is then observed after the end of the 60–50 ka low dust interval, reaching a maximum (∼1.6 g cm^{-2} kyr^{-1}) at 35 to 33 ka. Millennial-scale variability is superimposed on this broad trend, including peaks in flux coincident with H5 and H4. Dust fluxes decrease from the late MIS 3 maximum to ∼1 g cm^{-2} kyr^{-1} at the end of the LGM, with millennial-scale abrupt peaks in flux of 1.6 g cm^{-2} kyr^{-1} and 1.8 g cm^{-2} kyr^{-1}, coincident with H3 and H2 respectively. Following the LGM, the remainder of the record from this site is a detrital flux record (Adkins et al., 2006), as grain size-based estimates of the aeolian fraction of detrital sediments are not available. Although this may preclude direct quantitative comparison with the new dust flux data, the general trends in detrital flux can still be interpreted and compared to the dust flux data. This is evidenced by the consistent general trends between the dust flux and detrital flux records from 67 to 19 ka, spanning a similar range of detrital fluxes as found in the 19 ka to coretop portion of the record (Figure 3). Detrital fluxes rise to millennial-scale peaks during early H1 (1.7 g cm^{-2} kyr^{-1}) and the YD (2.1 g cm^{-2} kyr^{-1}) before decreasing to sustained low values (0.7–1 g cm^{-2} kyr^{-1}) during the AHP; a hiatus occurs from ∼17.5 to ∼15 ka, meaning flux data does not exist for the latter part of H1. Detrital fluxes increase abruptly at 5 ka and continue to rise steadily into the late Holocene to a value of ∼2 g cm^{-2} kyr^{-1}.

Both opal and organic carbon fluxes are positively correlated with dust fluxes in core ODP 658C ($r^2 = 0.46$; p-value < 0.05 and $r^2 = 0.32$; p-value < 0.05, respectively). Both opal and organic carbon fluxes increase from moderate values at the end of MIS 4 to two peaks coincident with H6 and H5a separated by an interval of lower fluxes, with the organic carbon showing higher amplitude rises and falls during the interval of lower fluxes. Biogenic fluxes variably rise and fall from H5a until ∼45 ka when both opal and organic carbon fluxes gradually increase to a maximum at 38 to 34 ka. Both opal and organic carbon fluxes drop sharply at 33 ka and remain low throughout MIS 2 and the LGM, with small peaks at H3 and H2. The opal flux record shows peaks during late H1 and the YD, falls to low levels throughout the AHP, and rises during the late Holocene. From the end of the LGM to the Holocene organic carbon concentrations have not been measured.

4. Discussion

4.1. Coherence of African Margin and Mid-Atlantic Dust Flux Records

This work has extended the CHEETA dust flux records to the bottom of cored material reaching back to 37 ka in GC37, 36.5 ka in GC49, and 26.5 ka in GC68, and produced a dust flux record from 67 to ∼19 ka for the core from ODP Hole 658C (Figure 3). The portions of the dust flux records from the ODP 658C, GC37, and GC49 sites that overlap in time from ∼37 to 20 ka demonstrate similar variation on both orbital and millennial timescales. In ODP 658C, dust flux increases are observed in the latter stages of Heinrich events 2 and 3 superimposed on a decreasing trend of dustiness through the end of the LGM. The GC68 record also shows an increase in dust flux associated with H2 timing, in the early stage of the event, and a decreasing trend of dustiness through the end of the LGM, with abrupt peaks in dust flux at ∼24 ka and ∼21.5 ka. In the northern core sites (ODP 658C through GC37, 21°–27°N), peak dust fluxes in early MIS 2 (27–23 ka) are similar to modern, and only in the southernmost core site (GC68, 19°N) are early MIS 2 fluxes higher than modern (by ∼50%). In all cores, dust fluxes drop from early MIS 2 to the LGM (23–19 ka) by 20%–40%. The overall agreement between dust records from 37 to 19 ka gives us confidence that the extended ODP 658C record from 67 to 37 ka is faithfully recording the export of dust to the margin.

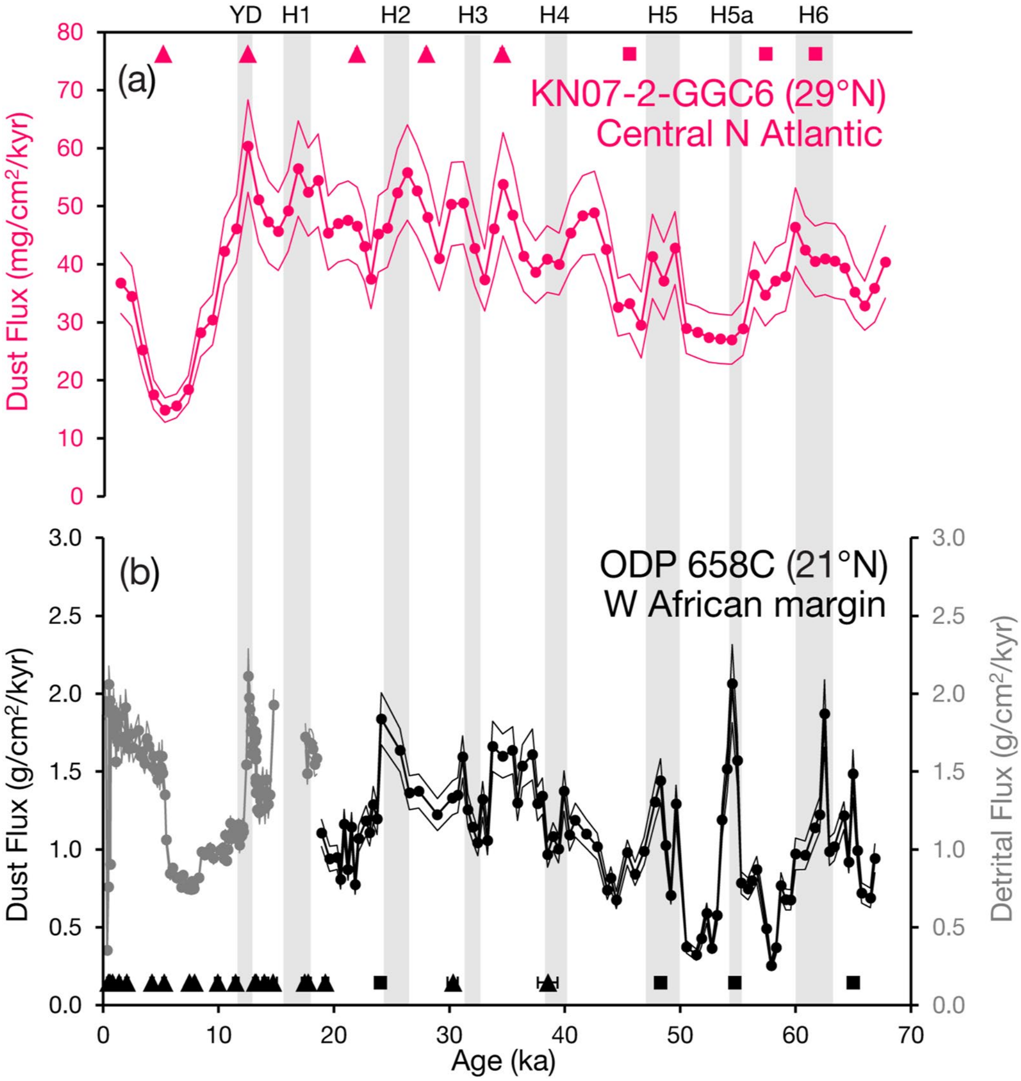

Figure 4. Comparison of central N Atlantic and W African margin dust records. (a) KN207-2-GGC6 3pt temporally smoothed dust flux record (pink circles) with 1σ uncertainty and age control (^{14}C tie points shown as pink triangles with 1σ uncertainties smaller than the width of the tie point markers, calcium carbonate stratigraphy tie points shown as pink squares) from the central N Atlantic (Middleton et al., 2018). (b) ODP 658C dust and detrital flux records (black and gray circles, respectively) with 1σ uncertainty and age control (^{14}C tie points shown as black triangles with 1σ uncertainties, calcium carbonate stratigraphy tie points shown as black squares) from the W African margin. Flux data <19 ka from Adkins et al. (2006) and ^{14}C tie points <20 ka from deMenocal, Ortiz, Guilderson, Adkins, et al. (2000) and deMenocal, Ortiz, Guilderson, and Sarnthein (2000). Vertical bars show time intervals of comparison between the records (YD—Rasmussen et al., 2006; H1-6 timing—Sánchez Goñi & Harrison, 2010; H5a timing—Rashid et al., 2003; H5a relative timing—Seierstad et al., 2014).

The ODP 658C record shows similarity to the dust flux record covering the last 67 ka from the Mid-Atlantic at 29°N (Middleton et al., 2018), both in overall trends and millennial-scale variability (Figure 4). Both records exhibit a background increase in dustiness throughout MIS 3, a large decrease during the AHP, and peaks in dust flux during Heinrich events. There are two distinct times of disagreement between the records, namely during the AHP through the late Holocene, and from 60 to 50 ka. In the Mid-Atlantic record, the AHP has a more gradual onset and ends 2 kyr later than in the ODP 658C record. However only two age tie points constrain the Mid-Atlantic dust record over the last 20 ka making comparison to the ODP 658C dust record challenging, which is highly constrained by eighteen ^{14}C tie points over the same time interval (Figure 4). From 60 to 50 ka the ODP 658C record exhibits much higher variability with fluxes reaching both their maximum and minimum levels of the whole 67 ka record. These disagreements are likely a consequence of low sedimentation rates at the

Mid-Atlantic site (averaging 2 cm/kyr), whereas the ODP 658C site has an average sedimentation rate of 13 cm/kyr. The high amplitude and abrupt changes in dust flux during the AHP and the 60 to 50 ka humid period are well resolved due to the high sedimentation rates at the ODP 658C site, whereas the amplitude of these abrupt changes may have been smoothed due to the much lower sedimentation rate and thus greater influence of mixing by bioturbation at the Mid-Atlantic site.

The agreement with the Mid-Atlantic dust record, which lies thousands of miles downwind of African dust sources, is important in that the Mid-Atlantic site is likely to be biased toward summer rather than winter dust emissions, and it presumably reflects dust from a wider region of North Africa than the margin sites. We assume that the winter and summer dust plumes largely follow the same routes as in the modern, and hence that the seasons represented by each site has been constant through the past 67 ka. The latitude of the Mid-Atlantic dust record (29°N) is 11° further north than the modern day core of the summer dust plume meaning that drastic latitudinal movement of the plume would be necessary to alter the season it represents, which is not supported by data (Sarnthein et al., 1981) or modeling (Albani et al., 2016). The general trends of the dust record from the ODP 658C site are consistent with the more northerly GC37 record (27°N) over the past ~37 ka, which lies 9° further north than the modern day core of the summer dust plume, meaning that any latitudinal change in the boundary between the summer and winter dust plume location did not affect the seasonality of the GC37 site. We assume that this situation was also consistent over the 67 to 37 ka interval, which did not contain any larger shifts to the climate system than those seen in the most recent 37 ka. Consistent with previous work (Williams et al., 2016), this comparison between the African margin and the Mid-Atlantic sites suggests that the summer and winter dust plumes, and dust deposition at both proximal and distal sites, have largely varied in sync over the late Pleistocene. The agreement also builds confidence that the variations in sea-level (and thus in the distance to dust source areas) has not had a substantial influence on dust deposition at the margin sites. Therefore, the ODP 658C dust record appears to be representative of an integrated signal of African dust export to the North Atlantic over the past 67 ka.

4.2. Major Features of Dust Flux Records From 67 to 20 ka (MIS 4 Through 2)

We begin by describing the broader-scale features of the records before turning to millennial-scale variability. At the onset of MIS 3 (~60 ka) Northern Hemisphere temperatures increase, and during this time dust fluxes in ODP 658C drop to values comparable to those during the AHP (a direct comparison of dust fluxes is not possible because Adkins et al. (2006) reported total detrital fluxes, providing only an upper bound on dust fluxes). Over the next 30 kyr, Northern Hemisphere high-latitude temperatures reflected in Greenland ice core records decrease gradually to minimum values between 30 and 25 ka, with multiple millennial-scale stadials superimposed on the background decrease (Figure 5) (Seierstad et al., 2014). Dust fluxes over this interval show a gradual increase to sustained high values during the end of MIS 3 and early MIS 2, with millennial-scale pulses of high dust flux superimposed on the background increase.

During MIS 2, Northern Hemisphere high-latitude temperatures gradually increase after 24 ka leading into the LGM time slice commonly targeted for data-model comparisons (23–19 ka) (e.g., Waelbroeck et al., 2009). Dust fluxes over this interval decrease from the high values observed at 30 to 25 ka; as a result, in all but the southernmost core (GC68, 19°N) the LGM is characterized by dust deposition rates that are similar to late Holocene fluxes. The observed increase in the LGM to late Holocene dust flux ratio at the southern end of the transect is consistent with the map of dust flux ratios compiled by Rowland et al. (2021), which shows that LGM dust fluxes are roughly twice as high as late Holocene dust fluxes in sediment cores <10°N in the tropical Atlantic. The broad scale features of the dust records from the end of MIS 4 through the end of MIS 2 show a strong correspondence over this interval between high-latitude temperatures and dust fluxes to the margin, with lower temperatures associated with higher fluxes to the margin and higher temperatures associated with lower fluxes to the margin.

The high sedimentation rates and well-resolved radiocarbon-based age model for GC68 allows a more detailed comparison between dust flux variability and millennial-scale high-latitude climate records over the last 26 ka. The millennial-scale features in the GC68 dust flux record associated with high-latitude climate fluctuations during H1, the Bølling-Allerød warm period, and the YD, previously described by McGee et al. (2013), show strong coherence between North Atlantic stadials and high fluxes of dust to the West African margin. Comparison of the earlier highly resolved 26.5 to 20 ka portion of the GC68 flux record (Figure 6) with a proxy record of

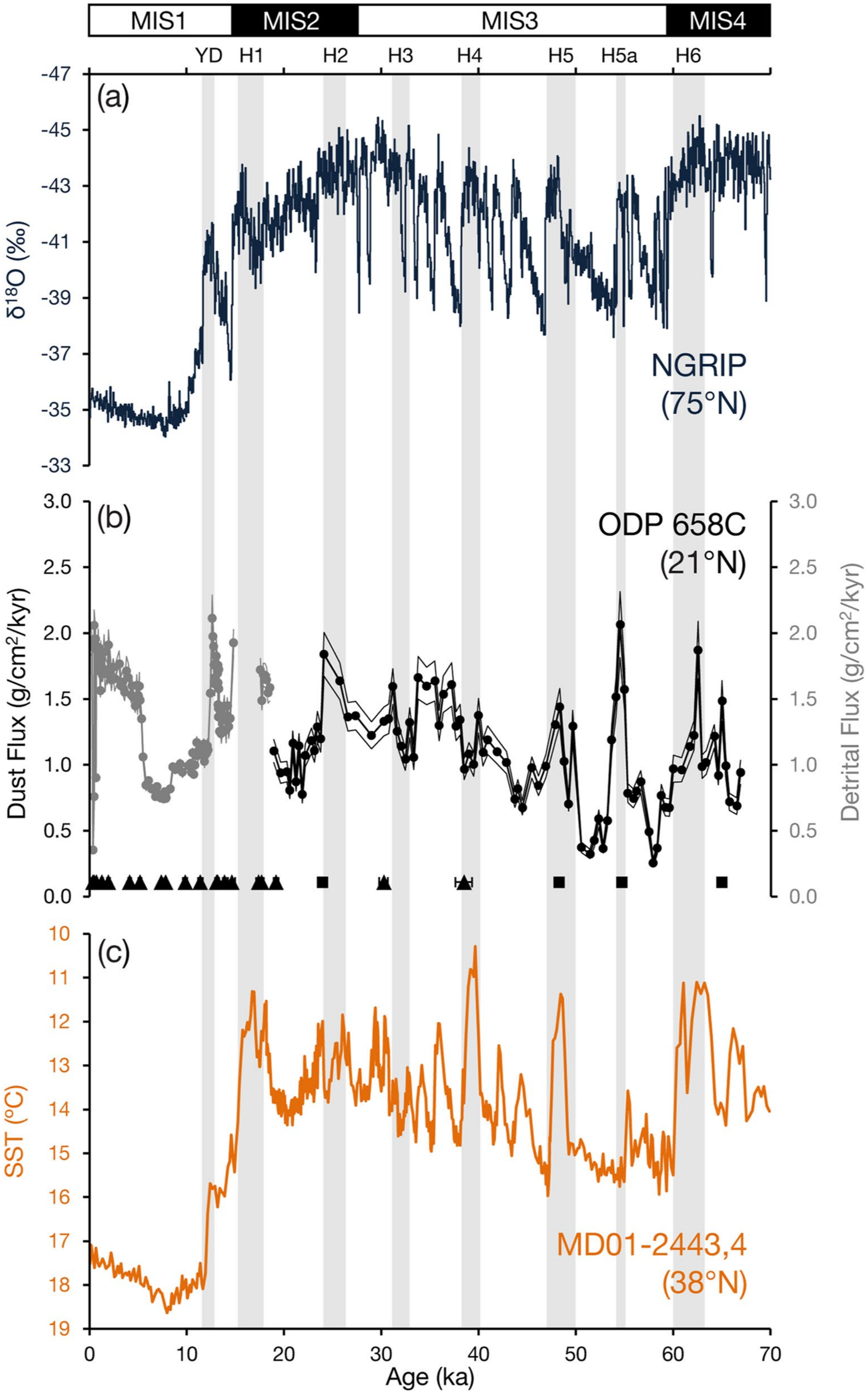
MIS1
MIS2
MIS3
MIS4
YD
H1
H2
H3
H4
H5
H5a
H6
(a)
δ18O (‰)
-47
-45
-43
-41
-39
-37
-35
-33
NGRIP
(75°N)
(b)
ODP 658C
(21°N)
Dust Flux (g/cm2/kyr)
Detrital Flux (g/cm2/kyr)
3.0
2.5
2.0
1.5
1.0
0.5
0.0
(c)
SST (°C)
10
11
12
13
14
15
16
17
18
19
MD01-2443,4
(38°N)
0
10
20
30
40
50
60
70
Age (ka)

Figure 5.

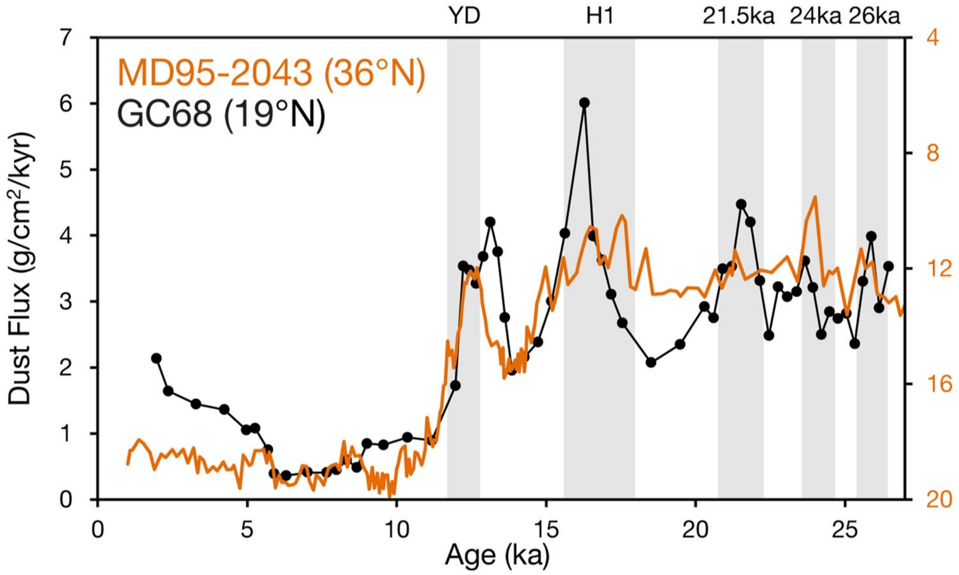

Figure 6. Comparison of N Atlantic SSTs and W African margin dust fluxes over the last 27 ka. GC68 dust flux record (black circles) and MD95-2043 SST record (orange line) (Cacho et al., 1999). Data <20 ka in GC68 from McGee et al. (2013). Vertical gray bars show time intervals of comparison between the records (YD—Rasmussen et al., 2006; H1—Sánchez Goñi & Harrison, 2010).

North Atlantic SSTs (Cacho et al., 1999) reveals that the three cold events centered at 26, 24, and 21.5 ka are all associated with increases of dust flux to the margin. The amplitudes of dust flux over this interval do not have a clear correspondence with amplitude of SST (i.e., the largest dust flux peak at 21.5 ka does not occur at the time of coldest SST at 24 ka), which could be caused by variable bioturbation and smoothing of the peaks in the two records.

While the GC68 cored material ends at 26.5 ka, the older material from CHEETA cores GC37 and GC49 and ODP Hole 658C shows peaks of dust flux likely associated with earlier millennial-scale North Atlantic stadial events (Figure 3). At 62.5 ka there is a pronounced stadial (including Heinrich event 6) in the North Atlantic with an accompanying millennial-scale peak in which dust fluxes at ODP 658C almost double. This signal of increased dust during stadials with associated Heinrich events is a robust response, with dust increases seen at all H events from H5a to H2. There are also stadial events (without accompanying Heinrich events) with pronounced dust flux peaks at 36.5 ka and 34.5 ka, showing that increased export of dust is observed during stadials both with and without Heinrich events. There are multiple instances in which stadials are observed in the SST record without discernible increases in dust flux (47 ka, 30 ka; Figure 5), perhaps due to age model error, or increased smoothing by bioturbation during times of lower sedimentation rates (see Figures S1 and S2a in Supporting Information S1).

Based upon the similarity in timing between millennial-scale peaks in dust flux in our most robust record (GC68) with stadials in the North Atlantic, we suggest that the millennial-scale peaks in the longer dust flux records (ODP 658C, GC49, GC37) correspond to the millennial-scale stadial events in the North Atlantic SST records, and that any mismatches are likely due to issues with smoothing and age control. This conclusion, which could be strengthened by additional records with consistently high accumulation rates as in CHEETA core GC68, suggests that the impact of Heinrich events on West African climate was largely stable across varying orbital configurations and ice sheet extents during MIS 2, 3, and 4.

Figure 5. North Atlantic stadials and W African margin dust fluxes. (a) NGRIP δ^{18}O record (blue line) (Seierstad et al., 2014). (b) ODP 658C dust and detrital flux records (black and gray circles, respectively) with 1σ uncertainty and age control (^{14}C tie points shown as black triangles with 1σ uncertainties, calcium carbonate stratigraphy tie points shown as black squares) from the W African margin. Flux data <19 ka from Adkins et al. (2006) and ^{14}C tie points <20 ka from deMenocal, Ortiz, Guilderson, Adkins, et al. (2000) and deMenocal, Ortiz, Guilderson, and Sarnthein (2000). (c) MD01-2443,4 SST record (orange line) (Martrat et al., 2007). Vertical bars show time intervals of comparison between the records (YD—Rasmussen et al., 2006; H1-6 and MIS timing—Sánchez Goñi & Harrison, 2010; H5a timing—Rashid et al., 2003; H5a relative timing—Seierstad et al., 2014).

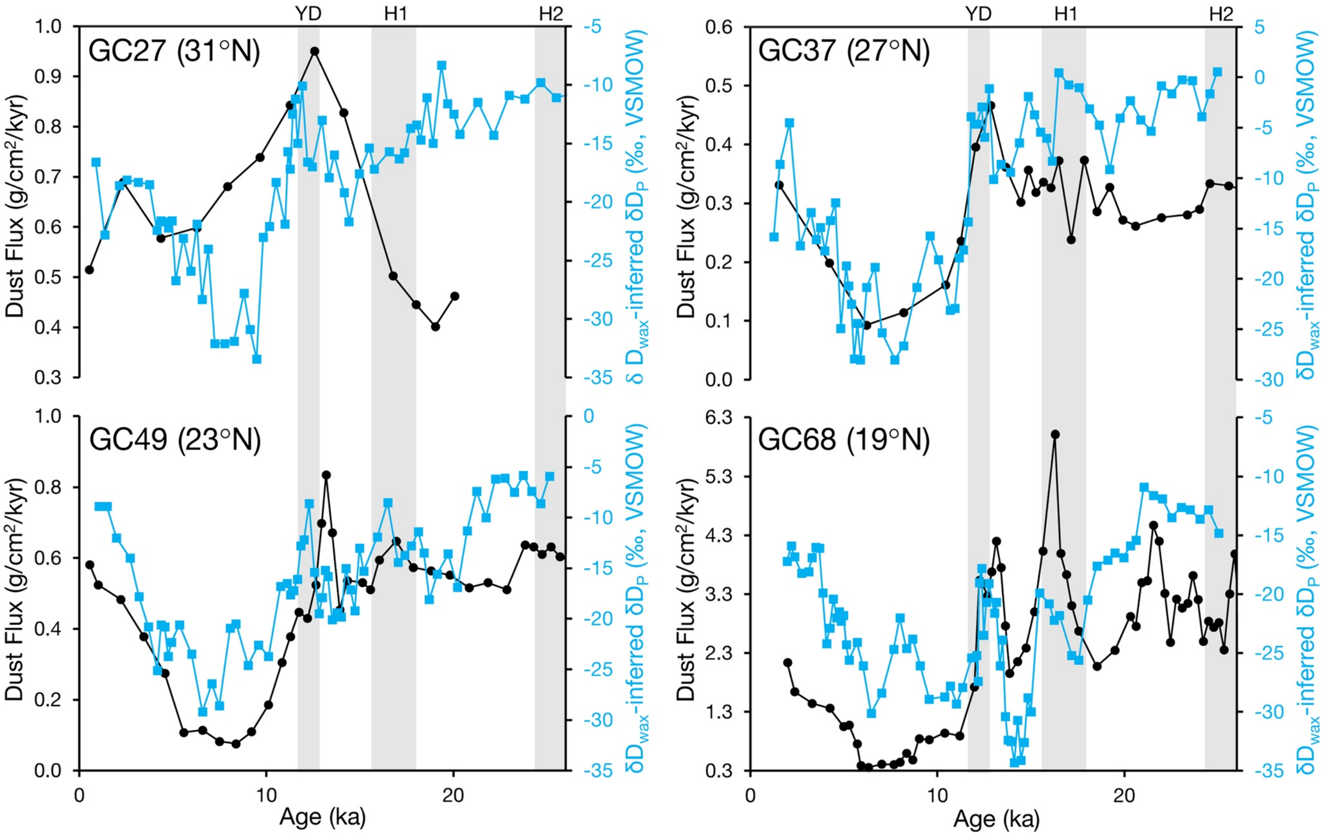

Figure 7. Comparison of dust flux and δD_P records along the W African margin. Dust flux records (black circles) and δD_{wax}-inferred hydrogen isotopic composition of precipitation records (δD_P) (blue circles) (Tierney, Pausata, & deMenocal, 2017) at CHEETA sites GC27, GC37, GC49, and GC68 as labeled. Flux data in GC27, <15 ka in GC37, <22 ka in GC49, and <20 ka in GC68 from McGee et al. (2013). Vertical gray bars show time intervals of comparison between the records (YD—Rasmussen et al., 2006; H events—Sánchez Goñi & Harrison, 2010).

4.3. Implications for Wind and Precipitation Changes Over North Africa During North Atlantic Cooling Events

These new data, in combination with previously published records, provide a clear picture of climate changes in stadial times in North Africa. First, it is clear that stadials are marked by both precipitation decreases and strengthening of northeasterly winds over North Africa. Stadials are marked by reduced precipitation in the Sahel and a southward shift of the Sahel/Sahara boundary (Collins et al., 2013; Weldeab et al., 2007). In the Sahara, leaf wax δD data from the CHEETA cores spanning the last 25 ka also document dry conditions in northwest Africa during stadial events (Tierney, Pausata, & deMenocal, 2017). However, northwest African margin δD values are no more positive during stadials than in the late Holocene (Figure 7), perhaps because precipitation cannot decrease much more than its current levels in the Sahara.

For the Saharan dust sources relevant for the northwest African margin and central Atlantic cores, increased aridity is thus unlikely to explain dust fluxes roughly double late Holocene values during stadials. Instead, Murphy et al. (2014) suggest that in areas that are already dry and dust producing like the Sahara, the only way to increase dust export is through an increase in wind speed; this conclusion is supported by studies supporting the dominant role of winds in modern decadal variability in Saharan dust emissions (Ridley et al., 2014; Wang et al., 2015). Consistent with this conclusion, our records show strong covariation of opal and organic carbon fluxes with dust fluxes throughout most of our records (Figure 2), providing firm evidence for intensification of northeasterly winds as a driver of increases in both coastal upwelling and dust deposition during stadials (Bradtmiller et al., 2016; McGee et al., 2018). There are other potential mechanisms which could explain the covariation of dust and organic carbon fluxes (ballasting of organic material by dust particles, e.g., van der Jagt et al., 2018) and the covariation of opal and organic carbon fluxes with dust fluxes (dust fertilization, e.g., Lambert et al., 2015), but a common control of upwelling and dust by near-surface northeasterly wind strength remains the more parsimonious interpretation of the data (Bradtmiller et al., 2016).

A modeling study by Liu et al. (2014) highlights the importance of these wind anomalies in communicating stadial conditions to the West African monsoon, demonstrating that anomalous northeasterly winds resulting from high-latitude cooling advect cold, dry air into North Africa, weakening the west African monsoonal circulation and drying the Sahel. This cold air advection is amplified by water vapor feedbacks, which further cool the Sahara and raise surface pressures, increasing northeasterly winds even more (Liu et al., 2014). Our dust and biogenic flux records thus provide support for Liu et al.'s ventilation mechanism as a driver of the reductions in Sahel rainfall suggested by proxy data during stadials (e.g., Weldeab et al., 2007). In stadials, as in modern decadal-scale variability (Wang et al., 2015), reduced Sahel precipitation occurs in association with strengthened northeasterly winds over the Sahara.

Combining West African margin dust flux and dust percentage data to form a north-south transect (Figure 8a), we also observe important latitudinal differences in the wind anomalies associated with different stadial events. These differences are most robust during H1 and the YD, periods for which dating uncertainties are relatively small and the most records exist. In records south of 20°N, dust increases during H1 are especially prominent, while dust changes during the YD are relatively muted. The opposite is true north of 20°N, as the YD dust flux peak is substantially greater than the H1 peak at 23°N and 27°N. Figure 8b shows a consistent increase in the YD:H1 dust flux ratio with increasing latitude. A weakness of our analysis of latitudinal variability is that we are comparing dust fluxes (which better represent dust deposition) and dust percentages. The dust percentage data was calculated by using an endmember unmixing analysis on the sediment major-element composition to separate dust, river-suspended, and marine-derived material, with the data represented as dust % = 100 * dust / (river + dust) (Collins et al., 2013), which may be impacted by changes in inputs of river-suspended material. This analysis could be improved by development of ^{230}Th-normalized dust flux records from the dust percentage records in Figure 8a. We note, however, that the pattern we identify—a decrease in the magnitude of Younger Dryas dust fluxes relative to H1 dust fluxes with decreasing latitude—is present in the flux records and does not depend on inclusion of the dust percentage records.

This observation suggests that northeasterly wind anomalies over North Africa peaked south of 20°N during H1, and north of 20°N during the YD. This different atmospheric response may reflect changing boundary conditions, in particular the effect of sea ice or land ice sheets (e.g., Chiang & Bitz, 2005; Chiang et al., 2003), where cooling of the NH is accompanied by southward shifts of the ITCZ and stronger trades (McGee et al., 2018). A decrease in ice sheets (in North America and Europe) and/or sea ice from H1 to the YD may therefore have caused a northward shift in the northeasterly wind anomalies over the West African margin. This difference in wind response would in turn imply differences in the wind-driven ocean circulation in the subtropical North Atlantic during the YD and H1.

4.4. Relationship Between Summer Insolation and NW African Climate During MIS 4 Through 2

In the new ODP 658C dust record extremely low dust fluxes are observed during the insolation maximum centered on 55 ka (Figure 9; low insolation values are oriented upwards). The values seen in terms of detrital flux are even lower than those recorded during the Green Sahara interval at 11 to 5 ka, where diverse proxy evidence indicates much higher rainfall supporting diverse vegetation, permanent lakes, and human populations (Gasse, 2000; Jolly et al., 1998; Kuper & Kröpelin, 2006; McGee & deMenocal, 2017; Tierney, Pausata, & deMenocal, 2017). Just as in the AHP, opal fluxes are low, suggesting reduced northwesterly wind strength during this wet period. The expression of the 60 to 50 ka low dust event differs from the AHP, however, in that it is punctuated by an abrupt millennial-scale increase in dust centered at 54.5 ka associated with H5a. Dust fluxes begin high at 60 ka (1.0 g cm^{-2} kyr^{-1}), decrease by a factor of three at 58 ka (0.3 g cm^{-2} kyr^{-1}), increase dramatically at 54.5 ka (2.1 g cm^{-2} kyr^{-1}), and decrease to minimum values again at 52 ka (0.3 g cm^{-2} kyr^{-1}), before increasing gradually throughout the next 15 kyr. This high dust flux event indicates that high-latitude climate can exert a strong influence on African climate even during a time of high summer insolation and a strong West African monsoon.

Comparison of the dust flux record at 60 to 50 ka with other paleoclimate archives of North African climate allows further probing of the structure of the Green Sahara event and how the interplay of high-latitude climate

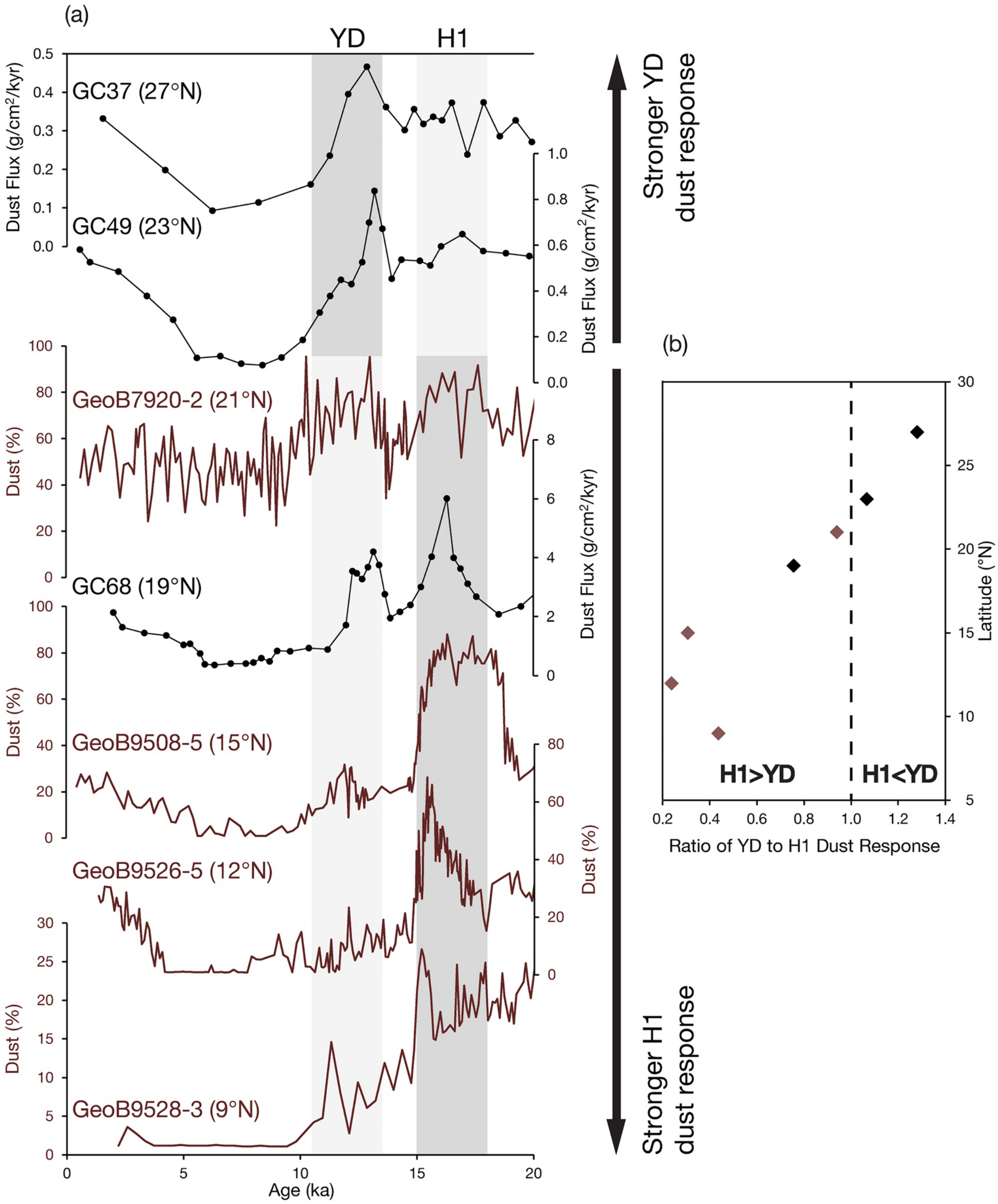

Figure 8. Latitudinal dust response at YD vs. H1 along the W African margin. (a) North to south transect of dust flux records (black circles) and dust percentage records (brown lines) (Collins et al., 2013) along the West African margin. Flux data <15 ka in GC37, and all flux data in GC49 and GC68 from McGee et al. (2013). Vertical gray bars shows a broad Younger Dryas interval (taken as 13.5–10.5 ka) and a broad Heinrich event 1 interval (taken as 18–15 ka). These intervals were chosen in order to encompass age model uncertainty between the records. Heavier shading of a vertical gray bar indicates the interval which has the largest relative dust response (YD or H1) within each dust record. (b) Ratio of the dust response during the Younger Dryas interval to the Heinrich event 1 interval versus latitude. The dashed vertical line separates the core sites with a larger dust response during the YD than during H1, from the core sites exhibiting a larger dust response during H1 than during the YD. All records were interpolated to a resolution of 0.1 kyr, and a ratio of YD to H1 dust response was calculated using the maximum value of the 0.5 kyr running means from each interval.

forcing with high summer insolation affects North African hydroclimate. The structure observed in the ODP 658C dust record is also observed in sea surface salinity (SSS) reconstructions in the eastern Gulf of Guinea, taken to reflect freshwater input from the Sanaga and Niger rivers (Weldeab et al., 2007), and grain size-based

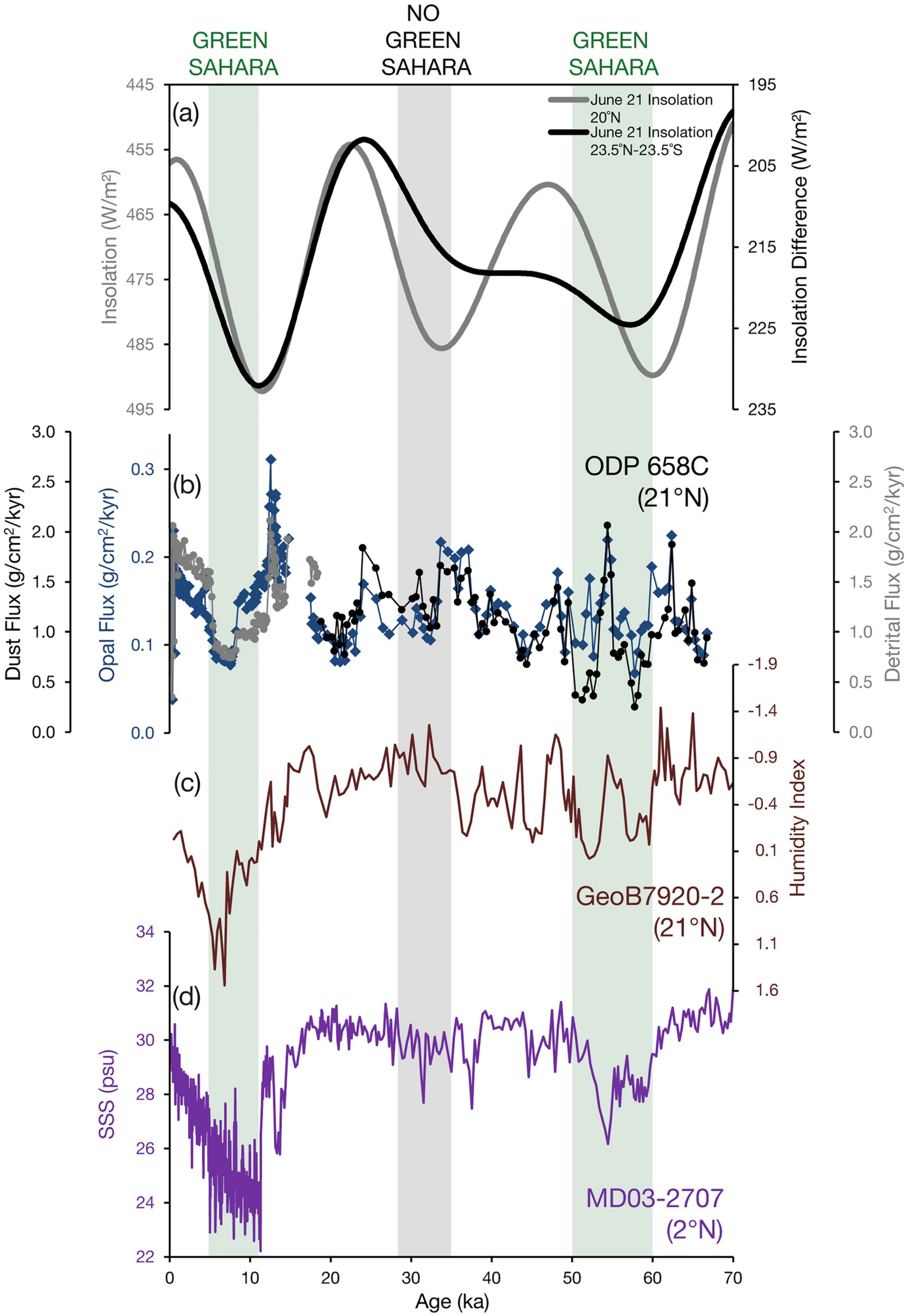
GREEN SAHARA
NO GREEN SAHARA
GREEN SAHARA
(a)
June 21 Insolation 20°N
June 21 Insolation 23.5°N-23.5°S
Insolation (W/m²)
445
455
465
475
485
495
Insolation Difference (W/m²)
195
205
215
225
235
(b)
ODP 658C (21°N)
Dust Flux (g/cm²/kyr)
0.0
0.5
1.0
1.5
2.0
2.5
3.0
Opal Flux (g/cm²/kyr)
0.0
0.1
0.2
0.3
Detrital Flux (g/cm²/kyr)
(c)
GeoB7920-2 (21°N)
Humidity Index
-1.9
-1.4
-0.9
-0.4
0.1
0.6
1.1
1.6
(d)
MD03-2707 (2°N)
SSS (psu)
22
24
26
28
30
32
34
Age (ka)
0
10
20
30
40
50
60
70

Figure 9.

continental humidity reconstructions off Cap Blanc (Tjallingii et al., 2008) suggesting a wetter tropical and subtropical North Africa. Wet conditions are also suggested by a low-resolution leaf wax record from ODP 659, which shows quite depleted δD values at ~50 ka (Kuechler et al., 2013).

The structure from 60 to 50 ka in the river discharge and humidity records differ somewhat from the dust record, as they show wetter conditions following the 54.5 ka stadial event, while the dust record shows equal magnitude dust flux minima preceding and following the stadial. Further, the salinity and grain size records both suggest that the 60 to 50 ka wet period was substantially drier than the Holocene AHP, while the detrital flux record of ODP 658C shows values during the 60 to 50 ka time slice comparable to that of the 11 to 5 ka interval. Future work will be required to explore the variable expression of this MIS 3 Green Sahara period in different regions of North Africa using different proxies, and the reason for the extreme expression of the AHP in many proxy records compared to earlier Green Sahara intervals. Potential avenues of exploration include effects of bioturbation, smoothing due to higher frequency climatic events in some intervals, and compaction of material downcore of the AHP leading to a bias in its expression compared to other wet periods.

Dust export to ODP 658C during the local summer insolation maximum from 35 to 28 ka has no discernible minimum in flux, as dust flux remains relatively high throughout this time, unlike the dust minima seen during the previous insolation maximum/Green Sahara interval from 60 to 50 ka, and the following insolation maximum/Green Sahara interval from 11 to 5 ka. The expression of this interval of insolation maximum (35–28 ka) in other records of North African hydroclimate is also as a time of aridity, with very high sea surface salinity (interpreted as low freshwater runoff from North Africa) in the Gulf of Guinea (Weldeab et al., 2007) and very low humidity index (interpreted as a high ratio of aeolian to fluvial sediments) in sediments near ODP 658C (Tjallingii et al., 2008). "Skipped beats" of insolation are similarly evident in the last two glacial periods in a dust flux record from the northwest African margin (Skonieczny et al., 2019) and a leaf wax δD record from East Africa (Tierney et al., 2017). In contrast, fluxes of C_{org} and opal decrease by a factor of ~2 over this time interval (Figure 9), but do not reach the minima observed in the Holocene and early MIS 3 Green Sahara intervals. This discrepancy, with dust fluxes staying relatively high throughout the insolation maximum while biogenic proxies decrease, may reflect a decrease in wind strength without a substantial decrease in aridity. Alternatively, the reduced biogenic fluxes may result from changes in the nutrient content of upwelled waters or effects on upwelling and productivity from changing shelf morphology due to sea-level lowering.

There are two possibilities to explain the "skipped beat" of insolation from 35 to 28 ka as expressed in North African hydroclimate records. The first is that high-latitude forcing during a time of high ice volume and cold temperatures may override the impact of increased summer heating of North Africa on the monsoon, keeping North Africa arid. The latter part of the 35 to 28 ka summer insolation maximum at 20°N is coincident with the coldest high-latitude temperatures during the past 70 ka as measured in Greenland ice, and the coldest sustained North Atlantic SSTs. The precessional beat of maximum local summer insolation thus occurs during a colder interval with higher ice volume than the preceding and subsequent Green Sahara intervals.

Alternatively, the second possibility is that the lack of response to high local summer insolation at 35 to 28 ka could be due to the fact that the precessional extreme occurs in association with low obliquity. As a result, high-latitude NH summer insolation and the cross-equatorial insolation gradient (calculated as the difference in June 21 insolation between 23.5°N and 23.5°S) remain low despite the maximum in 20°N summer insolation. We note that while much monsoon literature has focused on 65°N summer insolation, recent modeling experiments suggest that the cross-equatorial insolation gradient (which varies in phase with 65°N insolation) is more directly related to North African monsoon strength (Bosmans et al., 2015; Mantsis et al., 2014).

Modeling by Singarayer et al. (2017) appears to support the first suggestion of high ice volume and cold temperatures overriding the impact of increased summer heating of North Africa on the monsoon. In their simulations,

Figure 9. Green Sahara intervals in African climate proxy records over the last 70 ka. (a) June 21 insolation at 20°N (gray line) and cross-equatorial insolation gradient calculated as the difference in June 21 insolation between 23.5°N and 23.5°S (black line) (Laskar et al., 2004). (b) ODP 658C dust and detrital flux (black and gray circles, respectively) and opal flux (blue diamonds) records from the W African margin. Data <19 ka in ODP 658C from Adkins et al. (2006), deMenocal, Ortiz, Guilderson, Adkins, et al. (2000), and deMenocal, Ortiz, Guilderson, and Sarnthein (2000). (c) GeoB7920-2 Humidity Index record (brown line) (Tjallingii et al., 2008), with times of increased humidity of the African continent oriented downwards. (d) MD03-2707 sea surface salinity (SSS) record (purple line), taken to reflect freshwater input from the Sanaga and Niger rivers to the eastern Gulf of Guinea (Weldeab et al., 2007). Green vertical bars indicate Green Sahara intervals, with timing defined here by low detrital/dust fluxes in the ODP 658C record. The gray vertical bar indicates an interval of high June 21 insolation at 20°N that is not accompanied by a Green Sahara interval.

the summer rain belt over North Africa reaches similar latitudes during the summer insolation maxima at ∼35 and ∼55 ka when only orbital parameters and greenhouse gases are changed, but the rain belt is substantially farther south at 35 ka when ice sheets are included in the simulation.

5. Conclusions

Extended dust flux records from 19° to 27°N along the West African margin show a coherent signal of dust export during overlapping intervals, from 37 ka to present in cores GC37, GC49, and ODP 658C, and additionally in core GC68 from 26 ka to present. These records show a peak in dust at 35 to 33 ka, with fluxes decreasing toward the LGM; these multi-millennial trends appear to correlate with high-latitude temperature changes indicated by Greenland ice cores, with dust peaking during the coldest conditions. Due to the decline in dust fluxes in MIS 2, the LGM time slice commonly targeted in modeling experiments is marked by relatively moderate dust fluxes. The existence of LGM dust deposition similar to late Holocene levels in most cores despite the presence of large ice sheets and much steeper pole-to-equator surface temperature gradients is worthy of further investigation.

There is also coherent millennial-scale variability throughout our records. In core GC68, which has the highest accumulation rates and best-constrained age model in MIS 2, millennial-scale dust peaks correspond with reductions in North Atlantic SSTs. At other sites, most stadial events—including H2, H3, H4, H5, H5a, and H6—correspond to periods of high dust fluxes. Covariation of dust fluxes with fluxes of opal and organic carbon, taken here to represent coastal upwelling intensity, suggests that dust flux peaks during stadials are likely driven by increases in northeasterly wind strength. This finding provides support for the role of northeasterly winds in ventilating the West African monsoon during stadial events, leading to the observed decreases in Sahel precipitation. Examining a broad suite of dust records along the northwest African margin, we also find differences in wind anomalies associated with different stadials, with wind anomalies peaking south of 20°N during H1 and north of 20°N during the YD, perhaps due to changing ice sheet topography.

The longer dust flux record from ODP 658C reveals a Green Sahara interval at 60 to 50 ka marked by low dust fluxes. This period corresponds to a time of high NH summer insolation and relatively warm North Atlantic SSTs, suggesting a strong West African monsoon even in the presence of extended ice sheets and moderate atmospheric CO_2 concentrations. This interval differs from the AHP (11–5 ka), as there is a millennial-scale peak in dust flux during the interval that appears to correspond to H5a. The low-latitude summer insolation maximum at 35 ka is a “skipped beat,” in that there is no record of a strengthening of the west African monsoon and decrease in dust flux during this time, potentially due either to a reduced cross-equatorial insolation gradient during this time of low obliquity, or to the influence of cold North Atlantic temperatures and large ice sheets in counteracting the local insolation forcing on North African climate.

Data Availability Statement

The newly collected data associated with this manuscript are available for download from the National Oceanic and Atmospheric Administration National Centers for Environmental Information Paleoclimatology archive (https://www.ncdc.noaa.gov/paleo/study/33572) and described in Kinsley et al. (2021a). A compilation of all data (including previously published data) for the CHEETA core sites (GC37, GC49, and G68) and ODP Hole 658C are available for download from Zenodo (https://doi.org/10.5281/zenodo.5652188) and described in Kinsley et al. (2021b).

Acknowledgments
The authors would like to thank Irit Tal and Elena Steponaitis for laboratory assistance. The authors would also like to thank the crew, staff, and scientists of R/V Oceanus cruise 437-7, and co-chief scientists Tim Eglinton and Thomas Wagner. The sample material from the R/V Oceanus cruise 437-7 was provided by the Lamont-Doherty Core Repository of Lamont-Doherty Earth Observatory. The sample material from ODP Hole 658C was provided by the Ocean Drilling Program (ODP). This research was supported by NSF #OCE-1103262 to L. Bradtmiller, NSF #OCE-1030784 to D. McGee, P. deMenocal, and G. Winckler, and by internal grants from Macalester College and MIT. The authors gratefully acknowledge Anya Crocker and an anonymous reviewer for their constructive feedback.

References

Adkins, J., deMenocal, P., & Eshel, G. (2006). The “African humid period” and the record of marine upwelling from excess 230Th in Ocean Drilling Program Hole 658C. *Paleoceanography*, *21*(4), 1–14. https://doi.org/10.1029/2005PA001200

Albani, S., Mahowald, N. M., Murphy, L. N., Raiswell, R., Moore, J. K., Anderson, R. F., et al. (2016). Paleodust variability since the Last Glacial Maximum and implications for iron inputs to the ocean. *Geophysical Research Letters*, *43*(8), 3944–3954. https://doi.org/10.1002/2016GL067911

Andersen, M. B., Stirling, C. H., Zimmermann, B., & Halliday, A. N. (2010). Precise determination of the open ocean $^{234}U/^{238}U$ composition. *Geochemistry, Geophysics, Geosystems*, *11*(12), Q12003. https://doi.org/10.1029/2010GC003318

Bacon, M. P. (1984). Glacial to interglacial changes in carbonate and clay sedimentation in the Atlantic Ocean estimated from 230Th measurements. *Chemical Geology*, *46*(2), 97–111. https://doi.org/10.1016/0009-2541(84)90183-9

Battisti, D. S., Ding, Q., & Roe, G. H. (2014). Coherent pan-Asian climatic and isotopic response to orbital forcing of tropical insolation. *Journal of Geophysical Research*, *119*(21), 11997–12020. https://doi.org/10.1002/2014JD021960

Bory, A. J.-M., & Newton, P. P. (2000). Transport of airborne lithogenic material down through the water column in two contrasting regions of the eastern subtropical North Atlantic Ocean. *Global Biogeochemical Cycles*, *14*(1), 297–315. https://doi.org/10.1029/1999gb900098

Bosmans, J. H. C., Drijfhout, S. S., Tuenter, E., Hilgen, F. J., & Lourens, L. J. (2015). Response of the North African summer monsoon to precession and obliquity forcings in the EC-Earth GCM. *Climate Dynamics*, *44*(1–2), 279–297. https://doi.org/10.1007/s00382-014-2260-z

Braconnot, P., Harrison, S. P., Kageyama, M., Bartlein, P. J., Masson-Delmotte, V., Abe-Ouchi, A., et al. (2012). Evaluation of climate models using palaeoclimatic data. *Nature Climate Change*, *2*(6), 417–424. https://doi.org/10.1038/nclimate1456

Bradtmiller, L. I., McGee, D., Awalt, M., Evers, J., Yerxa, H., Kinsley, C. W., & deMenocal, P. B. (2016). Changes in biological productivity along the northwest African margin over the past 20,000 years. *Paleoceanography*, *31*(1), 185–202. https://doi.org/10.1002/2015PA002862

Bronk Ramsey, C. (2008). Deposition models for chronological records. *Quaternary Science Reviews*, *27*(1–2), 42–60. https://doi.org/10.1016/j.quascirev.2007.01.019

Cacho, I., Grimalt, J. O., Pelejero, C., Canals, M., Sierro, F. J., Flores, J. A., & Shackleton, N. (1999). Dansgaard-Oeschger and Heinrich event imprints in Alboran Sea paleotemperatures. *Paleoceanography*, *14*(6), 698–705. https://doi.org/10.1029/1999PA900044

Carlson, T. N., & Prospero, J. M. (1972). The large-scale movement of Saharan air outbreaks over the Northern Equatorial Atlantic. *Journal of Applied Meteorology*, *11*, 283–297. https://doi.org/10.1175/1520-0450(1972)011<0283:tlsmos>2.0.co;2

Chiang, J. C. H., Biasutti, M., & Battisti, D. S. (2003). Sensitivity of the Atlantic Intertropical Convergence Zone to Last Glacial Maximum boundary conditions. *Paleoceanography*, *18*(4), https://doi.org/10.1029/2003PA000916

Chiang, J. C. H., & Bitz, C. M. (2005). Influence of high latitude ice cover on the marine Intertropical Convergence Zone. *Climate Dynamics*, *25*(5), 477–496. https://doi.org/10.1007/s00382-005-0040-5

Chiapello, I., Bergametti, G., Gomes, L., Chatenet, B., Dulac, F., Pimenta, J., & Suares, E. S. (1995). An additional low layer transport of Sahelian and Saharan dust over the north-eastern Tropical Atlantic. *Geophysical Research Letters*, *22*(23), 3191–3194. https://doi.org/10.1029/95GL03313

Collins, J. A., Govin, A., Mulitza, S., Heslop, D., Zabel, M., Hartmann, J., et al. (2013). Abrupt shifts of the Sahara-Sahel boundary during Heinrich stadials. *Climate of the Past*, *9*(3), 1181–1191. https://doi.org/10.5194/cp-9-1181-2013

Copernicus Climate Change Service (C3S). (2017). *ERA5: Fifth generation of ECMWF atmospheric reanalyses of the global climate*. Copernicus Climate Change Service Climate Data Store (CDS). Retrieved from https://cds.climate.copernicus.eu/cdsapp#!/home

deMenocal, P.B. (1995). Plio-Pleistocene African climate. *Science*, *270*(5233), 53–59. https://doi.org/10.1126/science.270.5233.53

deMenocal, P. B., Ortiz, J., Guilderson, T., Adkins, J., Sarnthein, M., Baker, L., & Yarusinsky, M. (2000). Abrupt onset and termination of the African Humid Period: Rapid climate responses to gradual insolation forcing. *Quaternary Science Reviews*, *19*(1–5), 347–361. https://doi.org/10.1016/S0277-3791(99)00081-5

deMenocal, P. B., Ortiz, J., Guilderson, T., & Sarnthein, M. (2000). Coherent high- and low-latitude climate variability during the Holocene warm period. *Science*, *288*(5474), 2198–2202. https://doi.org/10.1126/science.288.5474.2198

deMenocal, P. B., Ruddiman, W. F., & Pokras, E. M. (1993). Influences of high- and low-latitude processes on African Terrestrial Climate: Pleistocene Eolian records from Equatorial Atlantic Ocean Drilling Program Site 663. *Paleoceanography*, *8*(2), 209–242. https://doi.org/10.1029/93PA02688

Doherty, O. M., Riemer, N., & Hameed, S. (2012). Control of Saharan mineral dust transport to Barbados in winter by the Intertropical Convergence Zone over West Africa. *Journal of Geophysical Research*, *117*(19), https://doi.org/10.1029/2012JD017767

Drake, N. A., Blench, R. M., Armitage, S. J., Bristow, C. S., & White, K. H. (2010). Ancient watercourses and biogeography of the Sahara explain the peopling of the desert. *Proceedings of the National Academy of Sciences*, *108*, 1–462. https://doi.org/10.1073/pnas.1012231108

Friese, C. A., van Hateren, J. A. V., Vogt, C., Fischer, G., & Stuut, J.-B. W. (2017). Seasonal provenance changes in present-day Saharan dust collected in and off Mauritania. *Atmospheric Chemistry and Physics*, *17*, 10163–10193. https://doi.org/10.5194/acp-17-10163-2017

Gasse, F. (2000). Hydrological changes in the African tropics since the Last Glacial Maximum. *Quaternary Science Reviews*, *19*(1–5), 189–211. https://doi.org/10.1016/S0277-3791(99)00061-X

Gómez-Letona, M., Ramos, A. G., Coca, J., & Arístegui, J. (2017). Trends in primary production in the canary current upwelling system—A regional perspective comparing remote sensing models. *Frontiers in Marine Science*, *4*, 1–18. https://doi.org/10.3389/fmars.2017.00370

Hayes, C. T., Anderson, R. F., Fleisher, M. Q., Huang, K., Robinson, L. F., Lu, Y., et al. (2015). 230Th and 231Pa on GEOTRACES GA03, the U.S. GEOTRACES North Atlantic transect, and implications for modern and paleoceanographic chemical fluxes. *Deep-Sea Research Part II: Topical Studies in Oceanography*, *116*, 29–41. https://doi.org/10.1016/j.dsr2.2014.07.007

Holz, C., Stuut, J. B. W., & Henrich, R. (2004). Terrigenous sedimentation processes along the continental margin off NW Africa: Implications from grain-size analysis of seabed sediments. *Sedimentology*, *51*(5), 1145–1154. https://doi.org/10.1111/j.1365-3091.2004.00665.x

Holz, C., Stuut, J. B. W., Henrich, R., & Meggers, H. (2007). Variability in terrigenous sedimentation processes off northwest Africa and its relation to climate changes: Inferences from grain-size distributions of a Holocene marine sediment record. *Sedimentary Geology*, *202*(3), 499–508. https://doi.org/10.1016/j.sedgeo.2007.03.015

Jolly, D., Prentice, I. C., Bonnefille, R., Ballouche, A., Bengo, M., Brenac, P., et al. (1998). Biome reconstruction from pollen and plant macrofossil data for Africa and the Arabian peninsula at 0 and 6000 years. *Journal of Biogeography*, *25*(6), 1007–1027. https://doi.org/10.1046/j.1365-2699.1998.00238.x

Kinsley, C. W., Bradtmiller, L. I., McGee, D., Galgay, M., Stuut, J.-B., Tjallingii, R., et al. (2021a). *North African Dust Deposition Flux Data over the last 67,000 Years*. National Oceanic and Atmospheric Administration National Centers for Environmental Information Paleoclimatology Archive. https://www.ncdc.noaa.gov/paleo/study/33572

Kinsley, C. W., Bradtmiller, L. I., McGee, D., Galgay, M., Stuut, J.-B., Tjallingii, R., et al. (2021b). *Orbital- and Millennial-Scale Variability in Northwest African Dust Emissions Over the Past 67,000 years—Datasets*. Zenodo. https://doi.org/10.5281/zenodo.5652189

Kuechler, R. R., Schefuß, E., Beckmann, B., Dupont, L., & Wefer, G. (2013). NW African hydrology and vegetation during the Last Glacial cycle reflected in plant-wax-specific hydrogen and carbon isotopes. *Quaternary Science Reviews*, *82*, 56–67. https://doi.org/10.1016/j.quascirev.2013.10.013

Kuper, R., & Kröpelin, S. (2006). Climate-controlled Holocene occupation in the Sahara: Motor of Africa's evolution. *Science*, *313*(5788), 803–807. https://doi.org/10.1126/science.1130989

Kutzbach, J. E. (1981). Monsoon climate of the early Holocene: Climate experiment with the Earth's orbital parameters for 9000 years ago. *Science*, *214*, 59–61. https://doi.org/10.1126/science.214.4516.59

Lambert, F., Tagliabue, A., Shaffer, G., Lamy, F., Winckler, G., Farias, L., et al. (2015). Dust fluxes and iron fertilization in Holocene and Last Glacial Maximum climates. *Geophysical Research Letters*, *42*(14), 6014–6023. https://doi.org/10.1002/2015GL064250

Laskar, J., Robutel, P., Joutel, F., Gastineau, M., Correia, A. C. M., & Levrard, B. (2004). A long-term solution for the insolation quantities of the Earth. *Astronomy and Astrophysics*, (428), 261–285. https://doi.org/10.1051/0004-6361:20041335

Liu, Y., Chiang, J. C. H., Chou, C., & Patricola, C. M. (2014). Atmospheric teleconnection mechanisms of extratropical North Atlantic SST influence on Sahel rainfall. *Climate Dynamics*, *43*(9–10), 2797–2811. https://doi.org/10.1007/s00382-014-2094-8

Locarnini, R. A., Mishonov, A. V., Baranova, O. K., Boyer, T. P., Zweng, M. M., Garcia, H. E., et al. (2019). World Ocean Atlas 2018, Volume 1: Temperature. In A. Mishonov (Ed.), *NOAA Atlas NESDIS* (Vol. 81, p. 52). https://www.ncei.noaa.gov/products/world-ocean-atlas

Mantsis, D. F., Lintner, B. R., Broccoli, A. J., Erb, M. P., Clement, A. C., & Park, H. S. (2014). The response of large-scale circulation to obliquity-induced changes in meridional heating gradients. *Journal of Climate*, *27*(14), 5504–5516. https://doi.org/10.1175/JCLI-D-13-00526.1

Martrat, B., Grimalt, J. O., Shackleton, N. J., De Abreu, L., Hutterli, M. A., & Stocker, T. F. (2007). Four climate cycles of recurring deep and surface water destabilizations on the Iberian margin. *Science*, *317*(5837), 502–507. https://doi.org/10.1126/science.1139994

McGee, D., & deMenocal, P. B. (2017). *Climatic Changes and Cultural Responses During the African Humid Period Recorded in Multi-Proxy Data* (Vol. 1). Oxford University Press. https://doi.org/10.1093/acrefore/9780190228620.013.529

McGee, D., DeMenocal, P. B., Winckler, G., Stuut, J. B. W., & Bradtmiller, L. I. (2013). The magnitude, timing and abruptness of changes in North African dust deposition over the last 20,000yr. *Earth and Planetary Science Letters*, *371–372*, 163–176. https://doi.org/10.1016/j.epsl.2013.03.054

McGee, D., Marcantonio, F., McManus, J. F., & Winckler, G. (2010). The response of excess 230Th and extraterrestrial 3He to sediment redistribution at the Blake Ridge, western North Atlantic. *Earth and Planetary Science Letters*, *299*(1–2), 138–149. https://doi.org/10.1016/j.epsl.2010.08.029

McGee, D., Moreno-Chamarro, E., Green, B., Marshall, J., Galbraith, E., & Bradtmiller, L. (2018). Hemispherically asymmetric trade wind changes as signatures of past ITCZ shifts. *Quaternary Science Reviews*, *180*, 214–228. https://doi.org/10.1016/j.quascirev.2017.11.020

Meng, L., Gao, H. W., Yu, Y., Yao, X. H., Gao, Y., Zhang, C., & Fan, L. (2017). A new approach developed to study variability in North African dust transport routes over the Atlantic during 2001–2015. *Geophysical Research Letters*, *44*(1910), 026–10. https://doi.org/10.1002/2017GL074478

Meyer, I., Davies, G. R., Vogt, C., Kuhlmann, H., & Stuut, J. B. W. (2013). Changing rainfall patterns in NW Africa since the Younger Dryas. *Aeolian Research*, *10*, 111–123. https://doi.org/10.1016/j.aeolia.2013.03.003

Middleton, J. L., Mukhopadhyay, S., Langmuir, C. H., McManus, J. F., & Huybers, P. J. (2018). Millennial-scale variations in dustiness recorded in Mid-Atlantic sediments from 0 to 70 ka. *Earth and Planetary Science Letters*, *482*, 12–22. https://doi.org/10.1016/j.epsl.2017.10.034

Mortlock, R. A., & Froelich, P. N. (1989). A simple method for the rapid determination of biogenic opal in pelagic marine sediments. *Deep Sea Research Part A: Oceanographic Research Papers*, *36*(9), 1415–1426. https://doi.org/10.1016/0198-0149(89)90092-7

Mulitza, S., Heslop, D., Pittauerova, D., Fischer, H. W., Meyer, I., Stuut, J. B., et al. (2010). Increase in African dust flux at the onset of commercial agriculture in the Sahel region. *Nature*, *466*(7303), 226–228. https://doi.org/10.1038/nature09213

Mulitza, S., Prange, M., Stuut, J. B., Zabel, M., Von Dobeneck, T., Itambi, A. C., et al. (2008). Sahel megadroughts triggered by glacial slowdowns of Atlantic meridional overturning. *Paleoceanography*, *23*(4), https://doi.org/10.1029/2008PA001637

Murphy, L. N., Clement, A. C., Albani, S., Mahowald, N. M., Swart, P., & Arienzo, M. M. (2014). Simulated changes in atmospheric dust in response to a Heinrich stadial. *Paleoceanography*, *29*(1), 30–43. https://doi.org/10.1002/2013PA002550

Ndeye, M. (2008). Marine reservoir ages in northern Senegal and Mauritania coastal waters. *Radiocarbon*, *50*(2), 281–288. https://doi.org/10.1017/S0033822200033580

Pittauerov, D., Mulitza, S., Hettwig, B., Chehade, W., Stuut, J.-B., Mollenhauer, G., & Fischer, H. W. (2009). Application of self-absorption correction method in gamma spectroscopy for 210 Pb and 137 Cs sediment chronology on the continental slope off NW Africa. *Radioprotection*, *44*(5), 457–461. https://doi.org/10.1051/radiopro/20095085

Prospero, J. M., & Lamb, P. J. (2003). African droughts and dust transport to the Caribbean: Climate change implications. *Science*, *302*(5647), 1024–1027. https://doi.org/10.1126/science.1089915

Rashid, H., Hesse, R., & Piper, D. J. W. (2003). Evidence for an additional Heinrich event between H5 and H6 in the Labrador Sea. *Paleoceanography*, *18*(4), https://doi.org/10.1029/2003PA000913

Rasmussen, S. O., Andersen, K. K., Svensson, A. M., Steffensen, J. P., Vinther, B. M., Clausen, H. B., et al. (2006). A new Greenland ice core chronology for the last glacial termination. *Journal of Geophysical Research*, *111*, 1–16. https://doi.org/10.1029/2005JD006079

Ratmeyer, V., Balzer, W., Bergametti, G., Chiapello, I., Fischer, G., & Wyputta, U. (1999). Seasonal impact of mineral dust on deep-ocean particle flux in the eastern subtropical Atlantic Ocean. *Marine Geology*, *159*, 241–252. https://doi.org/10.1016/s0025-3227(98)00197-2

Reimer, P. J., Bard, E., Bayliss, A., Beck, J. W., Blackwell, P. G., Ramsey, C. B., et al. (2013). IntCal13 and Marine13 Radiocarbon Age Calibration Curves 0–50,000 Years cal BP. *Radiocarbon*, *55*(04), 1869–1887. https://doi.org/10.2458/azu_js_rc.55.16947

Ridley, D. A., Heald, C. L., & Ford, B. (2012). North African dust export and deposition: A satellite and model perspective. *Journal of Geophysical Research*, *117*(2), https://doi.org/10.1029/2011JD016794

Ridley, D. A., Heald, C. L., & Prospero, J. M. (2014). What controls the recent changes in African mineral dust aerosol across the Atlantic? *Atmospheric Chemistry and Physics*, *14*(11), 5735–5747. https://doi.org/10.5194/acp-14-5735-2014

Romero, O. E., Kim, J. H., & Donner, B. (2008). Submillennial-to-millennial variability of diatom production off Mauritania, NW Africa, during the last glacial cycle. *Paleoceanography*, *23*(3) https://doi.org/10.1029/2008PA001601

Rowland, G. H., Robinson, L. F., Hendry, K. R., Ng, H. C., McGee, D., & McManus, J. F. (2021). The spatial distribution of aeolian dust and terrigenous fluxes in the Tropical Atlantic Ocean since the Last Glacial Maximum. *Paleoceanography and Paleoclimatology*, *36*(2), 1–17. https://doi.org/10.1029/2020PA004148

Ruddiman, W., Sarnthein, M., Baldauf, J., Backman, J., Bloemendal, J., Curry, W., et al. (1988). *Proceedings of the Ocean Drilling Program Leg 108*. https://doi.org/10.2973/odp.proc.ir.108.1988

Sánchez Goñi, M. F., & Harrison, S. P. (2010). Millennial-scale climate variability and vegetation changes during the Last Glacial: Concepts and terminology. *Quaternary Science Reviews*, *29*(21–22), 2823–2827. https://doi.org/10.1016/j.quascirev.2009.11.014

Sarnthein, M., Tetzlaff, G., Koopmann, B., Wolter, K., & Pflaumann, U. (1981). Glacial and interglacial wind regimes over the eastern subtropical Atlantic and North-West Africa. *Nature*, *293*(5829), 193–196. https://doi.org/10.1038/293193a0

Scheuvens, D., Schütz, L., Kandler, K., Ebert, M., & Weinbruch, S. (2013). Earth-Science Reviews Bulk composition of northern African dust and its source sediments—A compilation. *Earth Science Reviews*, *116*, 170–194. https://doi.org/10.1016/j.earscirev.2012.08.005

Seierstad, I. K., Abbott, P. M., Bigler, M., Blunier, T., Bourne, A. J., Brook, E., et al. (2014). Consistently dated records from the Greenland GRIP, GISP2 and NGRIP ice cores for the past 104ka reveal regional millennial-scale δ18O gradients with possible Heinrich event imprint. *Quaternary Science Reviews*, *106*, 29–46. https://doi.org/10.1016/j.quascirev.2014.10.032

Singarayer, J. S., Valdes, P. J., & Roberts, W. H. G. (2017). Ocean dominated expansion and contraction of the late Quaternary tropical rainbelt. *Scientific Reports*, *7*(1), 1–9. https://doi.org/10.1038/s41598-017-09816-8

Skonieczny, C., Bory, A., Bout-Roumazeilles, V., Abouchami, W., Galer, S. J. G., Crosta, X., et al. (2013). A three-year time series of mineral dust deposits on the West African margin: Sedimentological and geochemical signatures and implications for interpretation of marine paleo-dust records. *Earth and Planetary Science Letters*, *364*, 145–156. https://doi.org/10.1016/j.epsl.2012.12.039

Skonieczny, C., McGee, D., Winckler, G., Bory, A., Bradtmiller, L. I., Kinsley, C. W., et al. (2019). Monsoon-driven Saharan dust variability over the past 240,000 years. *Science Advances*, *5*(1), eaav1887. https://doi.org/10.1126/sciadv.aav1887

Skonieczny, C., Paillou, P., Bory, A., Bayon, G., Biscara, L., Crosta, X., et al. (2015). African humid periods triggered the reactivation of a large river system in Western Sahara. *Nature Communications*, *6*, 6–11. https://doi.org/10.1038/ncomms9751

Stuut, J. B., Zabel, M., Ratmeyer, V., Helmke, P., Schefuß, E., Lavik, G., & Schneider, R. (2005). Provenance of present-day eolian dust collected off NW Africa. *Journal of Geophysical Research*, *110*(4), 1–14. https://doi.org/10.1029/2004JD005161

Suman, D. O., & Bacon, M. P. (1989). Variations in Holocene sedimentation in the North American Basin determined from230Th measurements. *Deep Sea Research Part A: Oceanographic Research Papers*, *36*(6), 869–878. https://doi.org/10.1016/0198-0149(89)90033-2

Sun, D. (2004). Monsoon and westerly circulation changes recorded in the late Cenozoic aeolian sequences of Northern China. *Global and Planetary Change*, *41*(1), 63–80. https://doi.org/10.1016/j.gloplacha.2003.11.001

Tierney, J. E., deMenocal, P. B., & Zander, P. D. (2017). A climatic context for the out-of-Africa migration. *Geology*, *45*(11), 1023–1026. https://doi.org/10.1130/G39457.1

Tierney, J. E., Pausata, F. S. R., & De Menocal, P. B. (2017). Rainfall regimes of the Green Sahara. *Science Advances*, *3*(1), 1–10. https://doi.org/10.1126/sciadv.1601503

Tjallingii, R., Claussen, M., Stuut, J. B. W., Fohlmeister, J., Jahn, A., Bickert, T., et al. (2008). Coherent high- and low-latitude control of the northwest African hydrological balance. *Nature Geoscience*, *1*(10), 670–675. https://doi.org/10.1038/ngeo289

van der Does, M., Korte, L. F., Munday, C. I., Brummer, G. J. A., & Stuut, J. B. W. (2016). Particle size traces modern Saharan dust transport and deposition across the equatorial North Atlantic. *Atmospheric Chemistry and Physics*, *16*(21), 13697–13710. https://doi.org/10.5194/acp-16-13697-2016

van der Jagt, H., Friese, C., Stuut, J.-B. W., Fischer, G., & Iversen, M. H. (2018). The ballasting effect of Saharan dust deposition on aggregate dynamics and carbon export: Aggregation, settling, and scavenging potential of marine snow. *Limnology and Oceanography*, *63*, 1386–1394. https://doi.org/10.1002/lno.10779

Waelbroeck, C., Labeyrie, L., Michel, E., Duplessy, J. C., McManus, J. F., Lambeck, K., et al. (2002). Sea-level and deep water temperature changes derived from benthic foraminifera isotopic records. *Quaternary Science Reviews*, *21*(1–3), 295–305. https://doi.org/10.1016/S0277-3791(01)00101-9

Waelbroeck, C., Paul, A., Kucera, M., Rosell-Melé, A., Weinelt, M., Schneider, R., et al. (2009). Constraints on the magnitude and patterns of ocean cooling at the Last Glacial Maximum. *Nature Geoscience*, *2*(2), 127–132. https://doi.org/10.1038/ngeo411

Wang, W., Evan, A. T., Flamant, C., & Lavaysse, C. (2015). On the decadal scale correlation between African dust and Sahel rainfall: The role of Saharan heat low-forced winds. *Science Advances*, *1*(9), 2010–2015. https://doi.org/10.1126/sciadv.1500646

Weldeab, S., Lea, D. W., Schneider, R. R., & Andersen, N. (2007). 155,000 years of West African monsoon and ocean thermal evolution. *Science*, *316*, 1303–1306. https://doi.org/10.1126/science.1140461

Weldeab, S., Menke, V., & Schmiedl, G. (2014). The pace of East African monsoon evolution during the Holocene. *Geophysical Research Letters*, *41*, 1724–1732. https://doi.org/10.1002/2014GL059361

Williams, R. H., McGee, D., Kinsley, C. W., Ridley, D. A., Hu, S., Fedorov, A., et al. (2016). Glacial to Holocene changes in trans-Atlantic Saharan dust transport and dust-climate feedbacks. *Science Advances*, *2*(11), 1–12. https://doi.org/10.1126/sciadv.1600445

Yu, H., Chin, M., Bian, H., Yuan, T., Prospero, J. M., Omar, A. H., et al. (2015). Quantification of trans-Atlantic dust transport from seven-year (2007–2013) record of CALIPSO lidar measurements. *Remote Sensing of Environment*, *159*, 232–249. https://doi.org/10.1016/j.rse.2014.12.010

Zobeck, T. M., Gill, T. E., & Popham, T. W. (1999). A two-parameter Weibull function to describe airborne dust particle size distributions. *Earth Surface Processes and Landforms*, *955*, 943–955. https://doi.org/10.1002/(SICI)1096-9837(199909)24:10<943::AID-ESP30>3.0.CO;2-9